

## CELLULAR NEUROSCIENCE

# Axonal transport of late endosomes and amphisomes is selectively modulated by local $\text{Ca}^{2+}$ efflux and disrupted by PSEN1 loss of function

Pearl P. Y. Lie<sup>1,2,†‡</sup>, Lang Yoo<sup>1,2,‡</sup>, Chris N. Goulbourne<sup>1</sup>, Martin J. Berg<sup>1</sup>, Philip Stavrides<sup>1</sup>, Chunfeng Huo<sup>1</sup>, Ju-Hyun Lee<sup>1,2</sup>, Ralph A. Nixon<sup>1,2,3,4\*</sup>

Dysfunction and mistrafficking of organelles in autophagy- and endosomal-lysosomal pathways are implicated in neurodegenerative diseases. Here, we reveal selective vulnerability of maturing degradative organelles (late endosomes/amphisomes) to disease-relevant local calcium dysregulation. These organelles undergo exclusive retrograde transport in axons, with occasional pauses triggered by regulated calcium efflux from agonist-evoked transient receptor potential cation channel mucolipin subfamily member 1 (TRPML1) channels—an effect greatly exaggerated by exogenous agonist mucolipin synthetic agonist 1 (ML-SA1). Deacidification of degradative organelles, as seen after Presenilin 1 (PSEN1) loss of function, induced pathological constitutive “inside-out” TRPML1 hyperactivation, slowing their transport comparably to ML-SA1 and causing accumulation in dystrophic axons. The mechanism involved calcium-mediated c-Jun N-terminal kinase (JNK) activation, which hyperphosphorylated dynein intermediate chain (DIC), reducing dynein activity. Blocking TRPML1 activation, JNK activity, or DIC1B serine-80 phosphorylation reversed transport deficits in *PSEN1* knockout neurons. Our results, including features demonstrated in Alzheimer-mutant *PSEN1* knockout mice, define a mechanism linking dysfunction and mistrafficking in lysosomal pathways to neuritic dystrophy under neurodegenerative conditions.

## INTRODUCTION

Vesicular axonal transport is impaired in multiple neurodegenerative diseases and contributes to pathogenesis (1–3), but the underlying mechanisms, including the relative contributions of malfunctioning transport machineries versus alterations in transported organelles, remain poorly understood. Axonal dystrophy is described under a growing number of neurodegenerative conditions promoted by lysosomal acidification deficits, including Alzheimer’s disease (AD) (4, 5), implicating axonal transport disruption and accumulation of organelles in autophagy- and endosomal-lysosomal degradative pathways. In axons, early endosomes and autophagosomes mature into late endosomes (LEs) and amphisomes, which undergo further maturation and simultaneous retrograde transport toward the perikarya where lysosomes are enriched (6–9). We recently showed that mature lysosomes with full degradative capability are restricted from axons and instead, trans-Golgi network (TGN)-derived transport carriers (TCs) are mobilized into axons, where they undergo bidirectional transport to supply lysosomal components to retrogradely transported pre-/partially degradative organelles for their maturation toward lysosomal identity (9). Without ready access to somal lysosomes, axonal autophagic vacuoles (AVs), LEs, and amphisomes have only partial degradative capability. Disruptions in retrograde transport of these organelles may thus lead to their massive accumulation in dystrophic swellings, a hallmark of many neurodegenerative diseases. Retrograde vesicular transport is mediated by the minus end-directed microtubule-based motor, cytoplasmic

dynein, which is stringently regulated and only undergoes processive movement when it is simultaneously bound to a proper cargo adaptor and its activator dynactin (10). In addition, phosphorylation of dynein components emerges as an important regulatory mechanism of dynein activity (11–14). Here, using Presenilin 1 (PSEN1)-deficient neurons as a model of lysosomal pH and calcium dysregulation (15, 16), we reveal a mechanism that links acidification deficit in axonal LEs/amphisomes to  $\text{Ca}^{2+}$ -mediated disruption of the phosphoregulation of dynein activity on these organelles. This mechanism accounts for cargo-specific transport stalling that yields the characteristic morphology of dystrophic neurites in AD.

PSEN1 is critical for the survival of neurons, and its loss of function mutations are the most common cause of early-onset familial AD (FAD) (17, 18). PSEN1 has multiple  $\gamma$ -secretase-independent functions (15, 16, 19–21) in addition to its role as the  $\gamma$ -secretase catalytic subunit (22). Notably, PSEN1 influences calcium homeostasis in multiple organelles (20), including lysosomes (16, 19), which are also a substantial store of intracellular  $\text{Ca}^{2+}$  (23, 24). We have linked PSEN1-dependent lysosomal acidification (15) to the maintenance of normal lysosomal calcium homeostasis (16). PSEN1 holoprotein assists the proper folding of the V0a1 subunit of vacuolar-type adenosine triphosphatase (vATPase) within the endoplasmic reticulum (ER), which is essential for subsequent V0a1 delivery via biosynthetic trafficking routes to lysosomes for the proper assembly of functional vATPase that mediates lysosomal acidification (15). In PSEN1 loss-of-function states, including PSEN1-FAD patient cells, *PSEN1* knockout (KO) and *PSEN1/PSEN2* double KO cells, and *PSEN1* hypomorphic mice, lysosome acidification deficit disrupts substrate degradation in autophagy- and endosomal-lysosomal pathways (15, 16, 25–28), which is reversed by reacidifying lysosomes with acidic nanoparticles or cyclic adenosine monophosphate-elevating agents (16, 28, 29). High lysosomal pH also induces hyperactivity of transient receptor potential cation channel mucolipin subfamily member 1 (TRPML-1) (30), triggering abnormal lysosomal  $\text{Ca}^{2+}$  efflux in PSEN1

<sup>1</sup>Center for Dementia Research, Nathan S. Kline Institute, Orangeburg, NY 10962, USA

<sup>2</sup>Department of Psychiatry, New York University Langone Medical Center, New York, NY 10016, USA. <sup>3</sup>Department of Cell Biology, New York University Langone Medical Center, New York, NY 10016, USA. <sup>4</sup>NYU Neuroscience Institute, New York University Langone Medical Center, New York, NY 10016, USA.

\*Corresponding author. Email: nixon@nki.rfmh.org

†Present address: PureTech Health, Boston, MA 02210, USA.

‡These authors contributed equally to this work as co-first authors.

Copyright © 2022 The Authors, some rights reserved; exclusive licensee American Association for the Advancement of Science. No claim to original U.S. Government Works. Distributed under a Creative Commons Attribution NonCommercial License 4.0 (CC BY-NC).

Downloaded from https://www.science.org at Nathan Kline Inst on April 29, 2022

loss-of-function states (16). Lysosomal dysfunction in FAD-linked *PSEN1* loss of function is irrelevant to  $\gamma$ -secretase activity (15), in contrast to the central role of altered  $\gamma$ -secretase activity in hidradenitis suppurativa, an inflammatory skin disease caused by mutations primarily in nicastrin and Presenilin enhancer, gamma-secretase subunit (*PSENEN*), and less frequently in *PSEN1* (31).

TRPML is a subfamily of  $\text{Ca}^{2+}$ -permeable LE/lysosomal cation channels that includes TRPML1 to TRPML3, but only TRPML1 shows robust expression in mammalian brains (32). Loss-of-function mutations in TRPML1 cause mucopolidosis type IV, a lysosomal storage disorder characterized by multiple neurological abnormalities (33). In addition, reduced TRPML1 expression or activity has been reported in experimental manipulations intending to model certain neurodegenerative diseases (34–36), leading to the development of therapeutic approaches using small-molecule TRPML agonists for compensating TRPML1 deficiency. In contrast to these models that may benefit from TRPML1 activation, pathological TRPML1 hyperactivity is found in *PSEN1* loss of function (16), resulting in excess cytosolic  $\text{Ca}^{2+}$  that has deleterious effects such as overactivation of calpains and kinases (37). Our present study characterizes the pathological role of hyperactive TRPML1-mediated  $\text{Ca}^{2+}$  efflux. We have defined the molecular mechanism that underlies axonopathy and formation of hallmark dystrophic neurites in familial AD caused by *PSEN1* loss of function and potentially in other neurodegenerative diseases involving dysfunction in lysosomal pathways.

## RESULTS

### TRPML1-mediated $\text{Ca}^{2+}$ efflux selectively modulates retrograde transport of LEs/amphisomes

Axonal LEs/amphisomes can be identified on the basis of their lysosomal-associated membrane protein 1 (LAMP1) positivity and significant acidification detectable by LysoTracker-red (LT) as we previously showed (9). We performed axonal transport studies in primary cultured neurons expressing LAMP1–yellow fluorescent protein (YFP) and colabeled with LT (Fig. 1, A to C). Motile vesicles were defined as having an average velocity of at least  $0.1 \mu\text{m/s}$  in either direction, and other vesicles below this threshold were collectively termed “nonmotile.” To investigate the effect of hyperactive TRPML1-mediated  $\text{Ca}^{2+}$  efflux on transport, we treated neurons with the synthetic agonist mucolipin synthetic agonist 1 (ML-SA1) that specifically activates TRPML subfamily members. In ML-SA1-treated neurons, the percentage of retrograde  $\text{LT}^+$  LAMP1 vesicles decreased by 61% with a commensurate increase in nonmotile vesicles (Fig. 1, A to C). This decrease in retrograde motility was caused by increased pausing, in terms of both pause time and pause frequency (Fig. 1C). Pause frequency of each vesicle was defined by the number of pauses divided by its total time spent moving, and therefore, this parameter was only applicable to vesicles with at least one motile segment (displacement of at least  $2 \mu\text{m}$  at a velocity of  $0.1 \mu\text{m/s}$  or above), whereas the percent time in pause applied to all vesicles including completely stationary ones. As a result of prolonged time in pause, average velocity and retrograde run length of these vesicles decreased significantly (Table 1). In contrast to ML-SA1’s notable effects on  $\text{LT}^+$  LAMP1 vesicles (i.e., LE/amphisomes), it induced only modest depression of retrograde motility in the  $\text{LT}^-$  LAMP1 vesicle subpopulation consisting mainly of TGN-derived TCs (Fig. 1C) (9). Despite the presence of TRPML1 in TCs (9), their substantially lower sensitivity to ML-SA1 as compared to LEs/amphisomes (Fig. 1C)

was presumably due to their incompatible membrane lipids for TRPML1 activation. LEs/amphisomes, but not TGN-derived vesicles, are enriched in the low abundance lipid phosphatidylinositol 3,5-bisphosphate (38, 39) that may play a permissive role in TRPML1 activation (40). In contrast to the inhibitory effect of TRPML1 hyperactivation on retrograde transport, blocking  $\text{Ca}^{2+}$  efflux in LEs/amphisomes modestly enhanced some aspects of their retrograde transport. In normal neurons treated with Ned-19, a nicotinic acid adenine dinucleotide phosphate analog that blocks TRPML1 hyperactivation (16),  $\text{LT}^+$  LAMP1 vesicles showed a mild reduction in their pause frequency (Fig. 1C) and an increase in retrograde run length (Table 1), but overall motility and percent time in pause were not significantly affected (Fig. 1C).

To confirm the effects of agonist-induced TRPML1 hyperactivation, we next used *PSEN1* KO as a different model in which impaired lysosomal acidification causes TRPML1 hyperactivity (16). We verified that *PSEN1* KO neurons exhibited phenotypes reflecting global acidification deficit in degradative organelles. These include the expected microtubule-associated protein 1A/1B-light chain 3 (LC3)-II accumulation, impaired cathepsin D maturation, decreased somal active cathepsin D and LT signals, and increased lysosomal pH (fig. S1, A to F). In addition, we noted an unexpected increase in lysosomal pH in ML-SA1-treated Ctrl neurons (fig. S1F). Consistent with measurements in whole neurons or in somas (fig. S1, A to F), the percentage of acidic LC3 vesicles in axons was lowered (fig. S1G).  $\text{Ca}^{2+}$  levels in the axoplasm of *PSEN1* KO neurons were significantly increased (fig. S1H), confirming previous observations in neuronal cell bodies (16). In addition, we did not detect significant change in levels of select  $\gamma$ -secretase subunits in *PSEN1* KO neurons (fig. S1I).

Similar to ML-SA1 treatment, *PSEN1* KO reduced the percentage of retrogradely moving  $\text{LT}^+$  LAMP1 vesicles by 55% and commensurately increased percentage of nonmotile vesicles (Fig. 1C). Moreover, percent time in pause and pause frequency (Fig. 1C) were both markedly increased, while retrograde run length and average velocity were significantly reduced (Table 1). By comparison, retrograde motility was much less impaired in  $\text{LT}^-$  LAMP1 vesicles (Fig. 1C), which consisted primarily of TCs in normal axons (9) but possibly included a minor fraction of deacidified LEs/amphisomes in *PSEN1* KO. Anterograde movement of  $\text{LT}^-$  LAMP1 vesicles was not detectably affected by either *PSEN1* KO or ML-SA1 treatment (Fig. 1C). These results demonstrated that transport deficits in ML-SA1-treated Ctrl neurons and those in *PSEN1* KO neurons were remarkably similar in terms of severity and selectivity toward LEs/amphisomes. We further demonstrated retrograde transport deficit of axonal LEs/amphisomes with another LE marker, Rab7, in *PSEN1* KO neurons (fig. S2). Slowed retrograde transport was associated with significant enlargement of LEs/amphisomes that occupied an increased axoplasmic volume (Table 1) and likely imposed a greater burden upon axons. Accumulation of stalled degradative organelles resulted in formation of focal swellings in dystrophic neurites in both ML-SA1-treated and *PSEN1* KO neurons (Fig. 1D). These swellings, averaging  $1.5 \mu\text{m}$  in diameter, contained primarily AV, LE, amphisomes, and autolysosomes. Furthermore, as a control condition, the transport of mitochondria, which lack TRPML1 channels, was not affected by *PSEN1* KO or ML-SA1 treatment in either direction (fig. S3, A to D).

Since lysosomal acidification deficit underlies TRPML1 hyperactivity in *PSEN1* KO neurons (16), we next assessed the axonal transport and acidification of LAMP1-mCherry vesicles that have taken up a mixture of dextrans conjugated to acid-insensitive

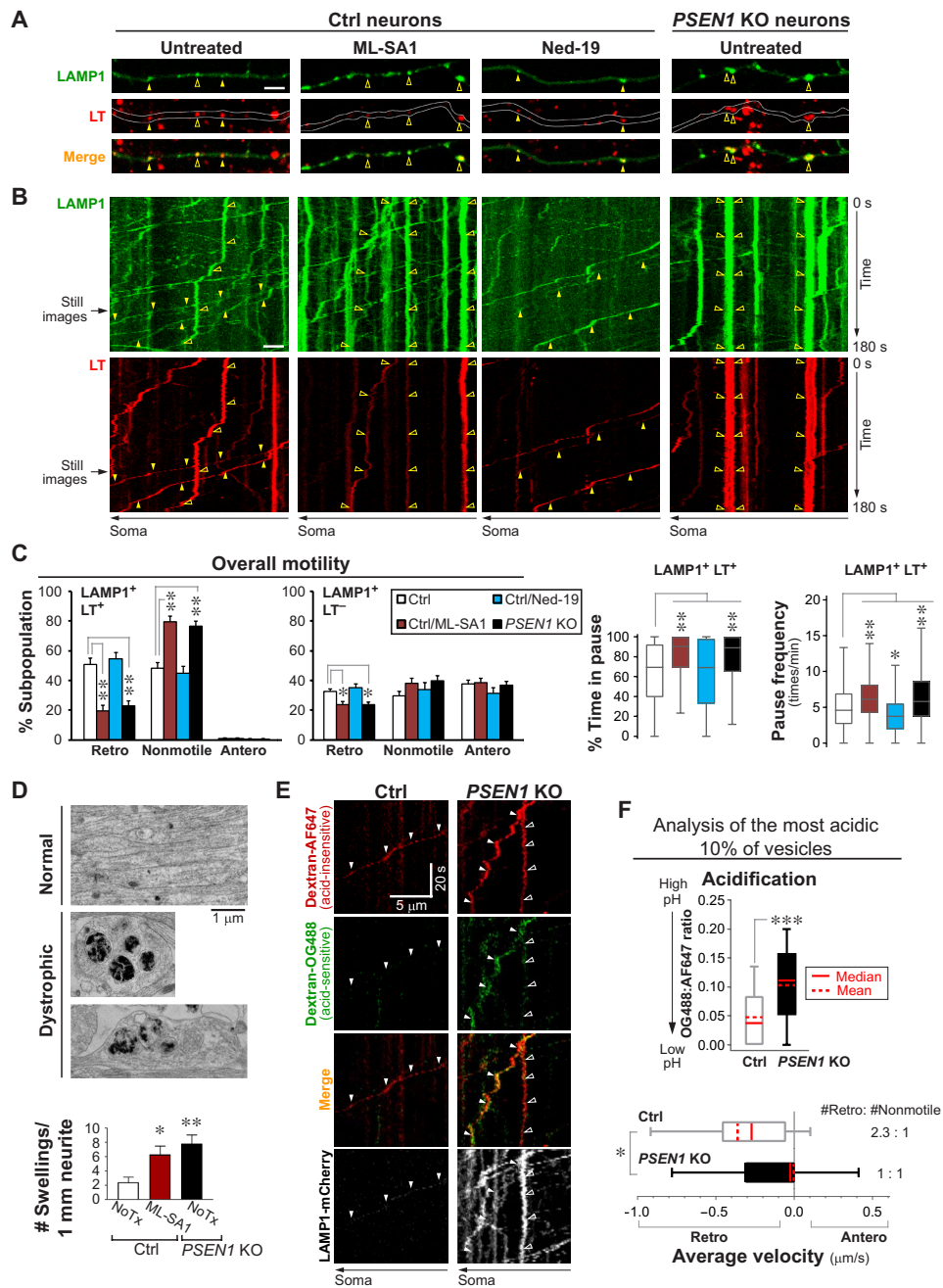


**Fig. 1. TRPML1-mediated Ca<sup>2+</sup> efflux selectively modulates retrograde transport of LEs/amphisomes.** (A to C) Time-lapse imaging in Ctrl axons ± ML-SA1 or Ned-19 treatment and *PSEN1* KO axons expressing LAMP1-YFP and colabeled with LT-Red. Scale bars, 5 μm. (A) Representative still images (left side; proximal to soma). Closed arrowheads, retrograde; open arrowheads, nonmotile. (B) Corresponding kymographs (time = 135 s). Arrowheads, trajectories of marked vesicles in (A). (C) Quantitative analyses. Overall motility: % retrograde (retro), nonmotile (<0.1 μm/s), and anterograde (antero) vesicles in LAMP1 vesicle subpopulations. Bars = means + SEM (n = 29, 21, 20, and 29 neurons). Percent time in pause of LAMP1<sup>+</sup> LT<sup>+</sup> vesicles is shown by Tukey's box-and-whisker plot (n = 462, 326, 293, and 380 vesicles). Pause frequency of LAMP1<sup>+</sup> LT<sup>+</sup> vesicles with at least one motile segment is shown by Tukey's box-and-whisker plot (n = 328, 152, 195, and 184 vesicles). \*P < 0.05 and \*\*P < 0.01 against Ctrl, Kruskal-Wallis test with Dunn's multiple comparisons. (D) Morphometric analysis of neurites in untreated (NoTx) or ML-SA1-treated Ctrl neurons and *PSEN1* KO neurons by electron microscopy. Representative images of normal and dystrophic neurites. Graph shows number of dystrophic swellings per 1 mm of neurites analyzed. Bars = means + SEM (n = 57 to 59 images per group; Ctrl and *PSEN1* KO data also shown in Fig. 7C). \*P < 0.05 and \*\*P < 0.01, Kruskal-Wallis test with Dunn's multiple comparisons. (E and F) Time-lapse imaging in LAMP1-mCherry-expressing Ctrl and *PSEN1* KO axons loaded with dextran-Alexa Fluor 647 (AF647) and dextran-Oregon Green 488 (OG488). (E) Representative kymographs. Closed arrowheads, retrograde; open arrowheads, nonmotile. (F) Quantitative analyses of the most acidic 10% of vesicles (LAMP1<sup>+</sup> AF647<sup>+</sup> OG488<sup>+/−</sup>) per group. Tukey's box-and-whisker plots show their acidification (OG488:AF647 ratio) and average velocity (n = 37 vesicles per group; individual data points, see fig. S4B). \*P < 0.05 and \*\*\*P < 0.001 against Ctrl, Mann-Whitney U test.

**Table 1. Effects of TRPML1-mediated Ca<sup>2+</sup> efflux on retrograde transport of LAMP1 vesicle subpopulations.** Time-lapse imaging was performed in 3-min intervals in axonal segments of untreated (NoTx), ML-SA1–treated or Ned-19–treated Ctrl neurons and in *PSEN1* KO neurons expressing LAMP1-YFP and colabeled with LT-Red. Table summarizes mean values of various parameters. For average velocities, negative values indicate retrograde direction. For retrograde segmental velocities, only vesicles with 1 or more retrograde segments of at least 2 μm were included. Antero, anterograde; retro, retrograde; vel., velocity.

	LAMP1 <sup>+</sup> LT <sup>+</sup>				LAMP1 <sup>+</sup> LT <sup>-</sup>			
	NoTx	ML-SA1	Ned-19	<i>PSEN1</i> KO	NoTx	ML-SA1	Ned-19	<i>PSEN1</i> KO
% of LAMP1 subpopulation	28.1	23.9	24.9	21.7	71.9	76.1	75.1	78.3
% Axoplasm occupied	6.1	7.8 <sup>#</sup>	5.7	7.7 <sup>#</sup>	6.6	11.1 <sup>#</sup>	7.6	10.9 <sup>#</sup>
<b>Non-antero vesicles</b>								
Diameter (μm)	0.768	0.923 <sup>**</sup>	0.791	0.928 <sup>**</sup>	0.567	0.712 <sup>**</sup>	0.575	0.704 <sup>**</sup>
Average vel. (μm/s)	-0.211	-0.084 <sup>**</sup>	-0.214	-0.100 <sup>**</sup>	-0.577	-0.389 <sup>**</sup>	-0.569	-0.370 <sup>**</sup>
Retro segmental vel. (μm/s)	0.573	0.495 <sup>*</sup>	0.545	0.526	1.145	0.989 <sup>**</sup>	1.098	1.011 <sup>**</sup>
Retro run length (μm)	6.6	3.5 <sup>**</sup>	8.2 <sup>*</sup>	4.0 <sup>**</sup>	12.5	10.1 <sup>**</sup>	12.3	9.1 <sup>**</sup>
% Time in pause (no./s)	63.5	79.9 <sup>**</sup>	62.6	79.0 <sup>**</sup>	50.6	60.6 <sup>**</sup>	51.0	61.9 <sup>**</sup>
Switch frequency (no./s)	0.017	0.013 <sup>*</sup>	0.012 <sup>**</sup>	0.015	0.022	0.021	0.022	0.022
No. of cells	29	21	20	29	29	21	20	29
No. of non-antero vesicles	456	322	291	378	739	598	597	883

<sup>#</sup>#*P* < 0.01, two-way ANOVA (no significant interaction between two factors: experimental group and LT positivity), followed by Dunnett's *t* test against untreated Ctrl. \**P* < 0.05 against untreated Ctrl, Kruskal-Wallis test with Dunn's multiple comparisons. \*\**P* < 0.01 against untreated Ctrl, Kruskal-Wallis test with Dunn's multiple comparisons.

and -sensitive dyes (Fig. 1, E and F), namely, Alexa Fluor 647 (AF647; acid insensitive) and Oregon Green 488 (OG488; quenched by acidic pH) (41). The most acidic 10% of vesicles were defined as the population of interest based on their exclusive retrograde motility in Ctrl axons, consistent with their identity as LEs/amphisomes (fig. S4A). In *PSEN1* KO axons, this vesicle population showed a significant increase in luminal pH as reflected by the increased ratio of OG488:AF647 signal intensity (Fig. 1F). Average velocity shifted from predominantly retrograde toward the nonmotile range, with the ratio of retrograde:nonmotile vesicles decreasing from 2.3:1 in Ctrl to 1:1 in *PSEN1* KO (Fig. 1F and fig. S4B).

### Blocking aberrant TRPML1-mediated Ca<sup>2+</sup> efflux rescues LE/amphisome retrograde transport impairment and neuritic dystrophy in *PSEN1* KO neurons

We previously demonstrated effective correction of lysosomal TRPML1 hyperactivity by treating *PSEN1* KO blastocysts with Ned-19 (16). Here, Ned-19 also blocked TRPML1 hyperactivity in axonal LEs/amphisomes (Figs. 2 and 3) without affecting Ca<sup>2+</sup> content in other organelles (fig. S3, E and F), thereby rescuing multiple axonal abnormalities in *PSEN1* KO neurons. Axonal transport study was performed in Ctrl, *PSEN1* KO, and Ned-19–treated *PSEN1* KO neurons expressing LAMP1-YFP and colabeled with LT (Fig. 2, A and B). As expected, Ned-19 was only effective in rescuing Ca<sup>2+</sup> dysregulation but not

acidification deficit (Fig. 2B) (16), as shown by the decreased LT positivity in axonal LAMP1 vesicles in *PSEN1* KO neurons with or without treatment. However, Ned-19 was able to override the primary deficit in acidification and completely restored LE/amphisome (LAMP1<sup>+</sup> LT<sup>+</sup>) retrograde transport in *PSEN1* KO back to the Ctrl level, as shown by the normalized percentages of retrograde and nonmotile vesicles and percent time in pause (Fig. 2B). The smaller decrements in retrograde transport of the LT<sup>-</sup> subpopulation were also reversed after Ned-19 treatment (Fig. 2B). Since Ned-19 can also target two pore channels (TPCs) (42), we knocked down TRPML1 by short hairpin RNA (shRNA) to further support the central role of TRPML1 but not TPCs in the pathobiology of *PSEN1* KO (Fig. 2, C to D), as we demonstrated previously in non-neuronal cells (16). Knockdown efficiency of TRPML1 was around 30%. In *PSEN1* KO neurons labeled with LT, transfection of shTRPML1-GFP normalized the increased pause frequency of LT vesicles back to the basal Ctrl level (Ctrl neurons transfected with nontargeting shRNA (shNeg)-GFP; Fig. 2D). In addition, notably, TRPML1 knockdown in Ctrl neurons further reduced LT vesicle pause frequency below the basal Ctrl level (Fig. 2D), similar to Ned-19-treated Ctrl neurons (Fig. 1C), further establishing a physiological regulation of Ca<sup>2+</sup> efflux influencing transport of LEs/amphisomes.

To directly visualize aberrant Ca<sup>2+</sup> efflux and transport impairment of LEs/amphisomes in *PSEN1* KO axons, we expressed a genetically

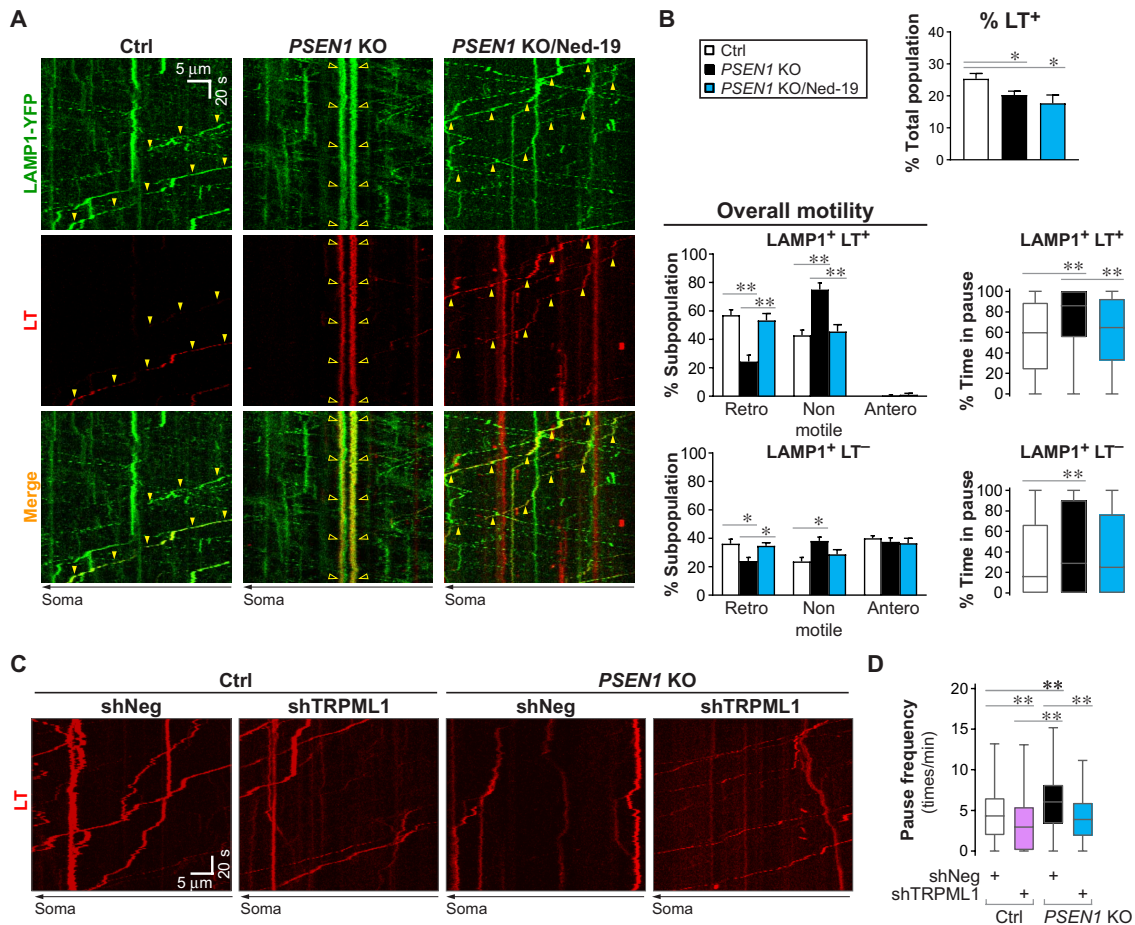


**Fig. 2. Blocking aberrant TRPML1-mediated Ca<sup>2+</sup> efflux rescues LE/amphisome retrograde transport impairment in *PSEN1* KO neurons.** (A and B) Time-lapse imaging in axonal segments of Ctrl neurons and untreated or Ned-19–treated *PSEN1* KO neurons expressing LAMP1-YFP and colabeled with LT-Red. (A) Representative kymographs are shown. Yellow arrowheads mark the trajectories of representative vesicles with both green (LAMP1) and red (LT) signals. Closed arrowheads, retrograde; open arrowheads, nonmotile. (B) Quantitative analyses of (A). Top graph shows % LT<sup>+</sup> vesicles in the total LAMP1 vesicle population. Bars = means + SEM (*n* = 45, 54, and 18 axons, respectively, in Ctrl, *PSEN1* KO, and *PSEN1* KO/Ned-19). Overall motility is represented by % retrograde (retro), nonmotile (<0.1 μm/s), and anterograde (antero) vesicles in each LAMP1 vesicle subpopulation. Bars = means + SEM (*n* = 11, 16, and 18 axons, respectively, in Ctrl, *PSEN1* KO, and *PSEN1* KO/Ned-19). Percent time in pause of LAMP1 vesicles in each subpopulation is shown by Tukey’s box-and-whisker plots (*n* = 109 LT<sup>+</sup> and 490 LT<sup>-</sup> vesicles, 215 LT<sup>+</sup> and 760 LT<sup>-</sup> vesicles, and 174 LT<sup>+</sup> and 845 LT<sup>-</sup> vesicles, respectively, in Ctrl, *PSEN1* KO, and *PSEN1* KO/Ned-19). (C and D) Time-lapse imaging in axonal segments of LT-labeled Ctrl and *PSEN1* KO neurons expressing shRNA-GFP plasmids: nontargeting (shNeg) or TRPML1 shRNA (shTRPML1). (C) Representative kymographs of LT signal are shown. (D) Pause frequency of LT vesicles with at least one motile segment is shown by Tukey’s box-and-whisker plot (*n* = 297, 400, 199, and 226 vesicles, respectively, in Ctrl/shNeg, Ctrl/shTRPML1, *PSEN1* KO/shNeg, and *PSEN1* KO/shTRPML1). (B and D) \**P* < 0.05 and \*\**P* < 0.01, one-way analysis of variance (ANOVA) with Tukey’s multiple comparisons or Kruskal-Wallis test with Dunn’s multiple comparisons.

encoded Ca<sup>2+</sup> indicator, GCaMP6m, conjugated to the cytoplasmic C terminus of LAMP1 (Fig. 3, A to C) in neurons coexpressing LAMP1-mCherry. As expected, percentage of axonal LAMP1 vesicles displaying Ca<sup>2+</sup> efflux (GCaMP<sup>+</sup>) markedly increased in *PSEN1* KO and was normalized to Ctrl level after Ned-19 treatment (Fig. 3C). Aberrant Ca<sup>2+</sup> efflux selectively impaired LE/amphisome retrograde motility, with concomitant increase in nonmotile GCaMP<sup>+</sup> vesicles and decrease in retrograde GCaMP<sup>-</sup> vesicles (Fig. 3C). These abnormalities were reversed by Ned-19 treatment. Notably, anterograde LAMP1 vesicles were largely GCaMP<sup>-</sup> (Fig. 3C), consistent with their expected identity as Golgi-derived TCs (9) that presumably lack TRPML1 activity, rather than LEs/amphisomes.

Impaired transport led to a greater volume of *PSEN1* KO axoplasm being occupied by LAMP1 vesicles that were increased both in size and in number (Table 2), and this was reversed by Ned-19 treatment (Table 2). We further investigated whether this accumulation

of axonal LEs/amphisomes was associated with the formation of neuritic dystrophy, a hallmark AD pathology. By electron microscopy, we surveyed the presence of dystrophic neurites in Ctrl and *PSEN1* KO neurons with or without Ned-19 treatment (Fig. 3D). The frequency of dystrophic neuritic swellings was significantly increased in *PSEN1* KO neurons, which was restored to the Ctrl level following Ned-19 treatment (Fig. 3D), supporting our hypothesis that the formation of AD pathology is accelerated by endosomal-lysosomal acidification deficit in *PSEN1* loss-of-function states in the presence of aging and other factors.

#### ***PSEN1* KO does not impair recruitment of dynein/dynactin and kinesin components on LEs/amphisomes and lysosomes**

To address the mechanism of defective retrograde transport of lysosomal pathway organelles caused by *PSEN1* KO, we first examined the levels of motor proteins recruited onto these organelles. We isolated

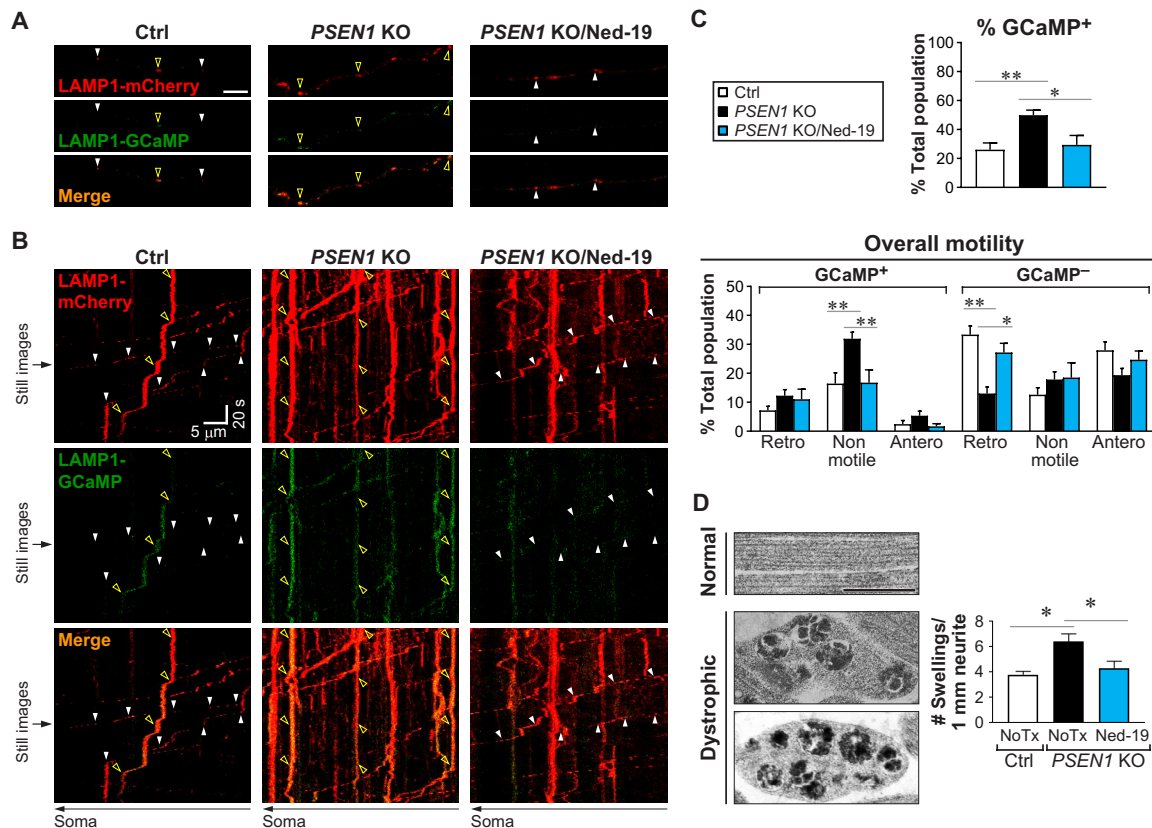


**Fig. 3. Blocking aberrant TRPML1-mediated  $\text{Ca}^{2+}$  efflux rescues LE/amphisome retrograde transport impairment and neuritic dystrophy in *PSEN1* KO neurons.** (A to C) Time-lapse imaging in axonal segments of Ctrl neurons and untreated or Ned-19–treated *PSEN1* KO neurons expressing LAMP1-mCherry and LAMP1-GCaMP. (A) Representative still images. Scale bar, 5  $\mu\text{m}$ . Yellow and white arrowheads respectively denote GCaMP<sup>+</sup> and GCaMP<sup>-</sup> LAMP1 vesicles. Closed arrowheads, retrograde; open arrowheads, nonmotile. (B) Representative kymographs corresponding to still images (A) (captured at time = 99 s). Arrowheads show trajectories of marked vesicles in (A). (C) Quantitative analyses of (B). Top graph shows % GCaMP<sup>+</sup> vesicles in the total LAMP1 vesicle population. Bars = means + SEM ( $n = 13, 14,$  and  $10$  axons, respectively, in Ctrl, *PSEN1* KO, and *PSEN1* KO/Ned-19). Overall motility is represented by % retrograde (retro), nonmotile ( $<0.1 \mu\text{m/s}$ ), and anterograde (antero) vesicles in the total LAMP1 vesicle population. Bars = means + SEM ( $n = 13, 14,$  and  $10$  axons, respectively, in Ctrl, *PSEN1* KO, and *PSEN1* KO/Ned-19). (D) Morphometric analysis of neurites in Ctrl and untreated (NoTx) or Ned-19–treated *PSEN1* KO neurons by electron microscopy. Representative images of normal and dystrophic neurites. Scale bar, 500 nm. Graph shows number of dystrophic swellings per 1 mm of neurites analyzed. Bars = means + SEM ( $n = 3$  independent experiments). (C and D)  $*P < 0.05$  and  $**P < 0.01$ , Kruskal-Wallis test with multiple comparisons (C) or one-way ANOVA with Dunnett's  $t$  test (D).

a subcellular fraction enriched in LEs/amphisomes and lysosomes, termed “LE-Lyso” fraction. This fraction was demonstrated to be highly enriched in lysosomal membrane proteins, cathepsin D, and related compartmental markers (fig. S1). Next, the levels of motor proteins (dynein/dynactin components, dynein accessory proteins, and kinesin components) associated with LEs/amphisomes and lysosomes were determined by immunoblotting and then normalized against the loading control lysosomal integral membrane protein 2 (LIMP2) (Fig. 4). In LE-Lyso fraction isolated from *PSEN1* KO neurons, pan dynein intermediate chain isoform 1/2 (DIC1/2) level remained unchanged, but we detected a 69% increase in DIC1 and a 63% increase in phosphorylated DIC (p-DIC) at S80 as compared to Ctrl neurons (Fig. 4B). DIC hyperphosphorylation will be further discussed in the next section. In addition, we observed a 90% increase in the dynein light chain LC8 (DYNLL1) and modest but significant increase in dynactin subunits p50 (36%) and Arp1 (28%) in the LE-Lyso fraction from *PSEN1* KO neurons (Fig. 4B). Levels of other examined proteins remained unaltered. These results indicate that defective transport of LEs/amphisomes in *PSEN1* KO axons was unlikely to be caused by a loss of association of motor proteins.

### DIC hyperphosphorylation mediates defective retrograde transport of LEs/amphisomes in *PSEN1* KO neurons

Simultaneous interaction of dynein, dynactin, and cargo is essential for activating processive minus-end directed movement of organelles (10). Given that we observed a prominent up-regulation of DIC1 in *PSEN1* KO (Fig. 4B) and that DIC is central to dynein-dynactin interaction via its direct binding with p150, we investigated the possibility of DIC misregulation by phosphorylation. The serine-rich region in DIC N terminus contains a cluster of phosphorylation sites conserved across all variants of both isoforms. Among these phosphorylation sites, S80 of the DIC1B neuronal specific variant has been reported to be phosphorylated for dynein recruitment to Rab7<sup>+</sup> endosomes (13), suggesting its possible role in regulating the transport of vesicles within the broader endosomal-lysosomal system. We first examined the phosphorylation status of this serine residue by performing immunostaining using an antibody specifically recognizing the phosphorylated epitope (fig. S4). For convenience, we will refer to this serine residue as S80 although the corresponding residue is at a different position in other DIC variants, e.g., S81 in ubiquitous DIC2C. Neurons were cultured in microfluidics devices to allow the

**Table 2. Summary of rescue effects in *PSEN1* KO neurons following various treatments.** nd, not determined.

	Ctrl	<i>PSEN1</i> KO		Treated <i>PSEN1</i> KO	
	Untreated	Untreated	Ned-19	DIC1B-S80A	L-JNKi
% Axoplasm occupied by LAMP1 vesicles*	34.9 ± 3.5	Increased; 58.0 ± 2.9**	Rescued; 40.6 ± 4.6##	nd	nd
Average diameter of LAMP1 vesicles† (μm)	0.60 ± 0.01	Increased; 0.67 ± 0.01**	Rescued; 0.61 ± 0.01#	Rescued; 0.58 ± 0.01##	Rescued; 0.59 ± 0.02##
Density of LAMP1 vesicles‡ in axons (number/1 mm axon)	153 ± 11	Increased; 212 ± 12**	Rescued; 157 ± 9##	nd	nd
Dystrophy		Increased; Figs. 1D and 3D	Rescued; Fig. 3D	nd	Rescued; Fig. 7C
% Retrograde LAMP1 vesicles		Decreased; Figs. 1 to 3, 5, and 7	Rescued; Figs. 2 and 3	Rescued; Fig. 5C	Rescued; Fig. 7B
% Pause time of LAMP1 vesicles		Increased; Table 1	Rescued; Fig. 2B	Rescued; Fig. 5C	Rescued; Fig. 7B
DIC phosphorylation level		Increased; Figs. 4 to 6	Rescued; Fig. 5E	nd	Rescued; Fig. 6I

\*Endogenous LAMP1 vesicles labeled by immunofluorescence staining; values = means ± SEM ( $n = 26, 35,$  and  $23$  axons, respectively) (see Figs. 4C and 5D). †Fluorescently tagged LAMP1 vesicles; values = means ± SEM ( $n = 47, 64, 34, 15,$  and  $21$  axons, respectively). ‡Fluorescently tagged LAMP1 vesicles; values = means ± SEM ( $n = 24, 30,$  and  $28$  axons, respectively). \*\* $P < 0.01$  against Ctrl. # $P < 0.05$  against *PSEN1* KO. ## $P < 0.01$  against *PSEN1* KO (Kruskal-Wallis test followed by Dunn's multiple comparison).

growth of axons through microgrooves that were 450 μm in length. Following coimmunostaining of DIC, p-DIC S80, and LAMP1, we captured images from the proximal 225-μm portion of microgrooves (Fig. 4C). The relative levels of DIC S80 phosphorylation were quantified on the basis of the ratio of p-DIC S80 to total DIC signal intensity. We observed a significantly increased DIC S80 phosphorylation level associated with LAMP1 vesicles in axons of *PSEN1* KO neurons than in Ctrl (Fig. 4D). Hyperphosphorylation of DIC S80 was associated with decreased retrograde motility, as we later showed (Fig. 5), implying a reduced dynein retrograde motor function despite increased DIC1 levels in LE-Lyso fraction of *PSEN1* KO neurons (Fig. 4B).

To investigate the role of DIC S80 hyperphosphorylation in defective LAMP1 vesicle retrograde transport, we examined the effects of expressing mCherry-tagged wild-type DIC1B and its S80 mutants (DIC1B-S80A, nonphosphorylatable; DIC1B-S80D, phosphomimetic) in *PSEN1* KO neurons coexpressing LAMP1-YFP (Fig. 5, A to C). We found that expression of the nonphosphorylatable mutant DIC1B-S80A fully restored normal LAMP1 vesicle retrograde motility (Fig. 5C), including normalized time spent pausing (Fig. 5C) and vesicle size (Table 2) in *PSEN1* KO neurons. By contrast, expression of wild-type DIC1B or phosphomimetic DIC1B-S80D did not restore LAMP1 vesicle motility in *PSEN1* KO neurons (Fig. 5C). In Ctrl neurons overexpressing DIC1B-S80D, retrograde transport of axonal LAMP1<sup>+</sup> LT<sup>+</sup> vesicles was significantly and selectively disrupted (fig. S6, A and B). These results support the hypothesis that hyperphosphorylation of DIC S80 in axons of *PSEN1* KO neurons or Ctrl neurons overexpressing DIC1B-S80D prevents the DIC dephosphorylation necessary to activate dynein motility on LE/amphisomes. We further showed that DIC S80 hyperphosphorylation was a result of LE/amphisomal Ca<sup>2+</sup> dysregulation by demonstrating the rescue effect of Ned-19 (Fig. 5, D and E). Neurons cultured in microfluidics devices were immunostained for DIC, p-DIC S80, and

LAMP1. Ned-19 treatment significantly lowered the DIC S80 phosphorylation level associated with axonal LAMP1 vesicles of *PSEN1* KO neurons, comparable to Ctrl neurons, and commensurately reduced the volume of LAMP1 vesicles in the axoplasm as estimated by the percentage of axonal length occupied (Table 2).

#### LE/amphisome retrograde transport impairment is dependent on c-Jun N-terminal kinase activation in *PSEN1* KO neurons

Because DIC S80 is a substrate of extracellular signal-regulated kinase (ERK) upon growth factor stimulation (13), we predicted that endosomal-lysosomal Ca<sup>2+</sup> efflux via TRPML1 might induce DIC hyperphosphorylation by members of the mitogen-activated protein kinase (MAPK) family (43, 44), which are predicted to phosphorylate DIC (45). Consistent with this possibility, we observed a ~3-fold increase in c-Jun N-terminal kinase (JNK) activation in *PSEN1* KO neurons, as reflected by an elevated phospho/total kinase ratio in immunoblot analyses of postnuclear supernatants (PNSs) from *PSEN1* KO and Ctrl neurons (Fig. 6, A and B). In addition, the level of p-JNK was increased twofold in the LE-Lyso fraction from *PSEN1* KO neurons (Fig. 6, A and C). By contrast, p-ERK levels in the LE-Lyso fraction of *PSEN1* KO neurons were not significantly altered, despite a minor increase in ERK activation in the PNSs (Fig. 6, A to C). To verify that TRPML1 hyperactivation in *PSEN1* KO neurons causes JNK hyperactivity, which, in turn, leads to DIC-S80 hyperphosphorylation, we performed immunoblotting of membrane preparations from *PSEN1* KO neurons following treatments with Ned-19 or L-JNKi (Fig. 6, E to G), a peptide inhibitor that specifically inhibits JNK activity without affecting ERK or p38 (46). As expected, both JNK and DIC hyperphosphorylation were blocked by TRPML1 inhibition (Fig. 6, D and E), and DIC hyperphosphorylation was blocked by JNK inhibition (Fig. 6, F and G). By immunostaining, we further showed that JNK inhibition restored the ratio of p-DIC/DIC signal intensities associated with axonal LAMP1 in *PSEN1* KO neurons (Fig. 6, H and I).

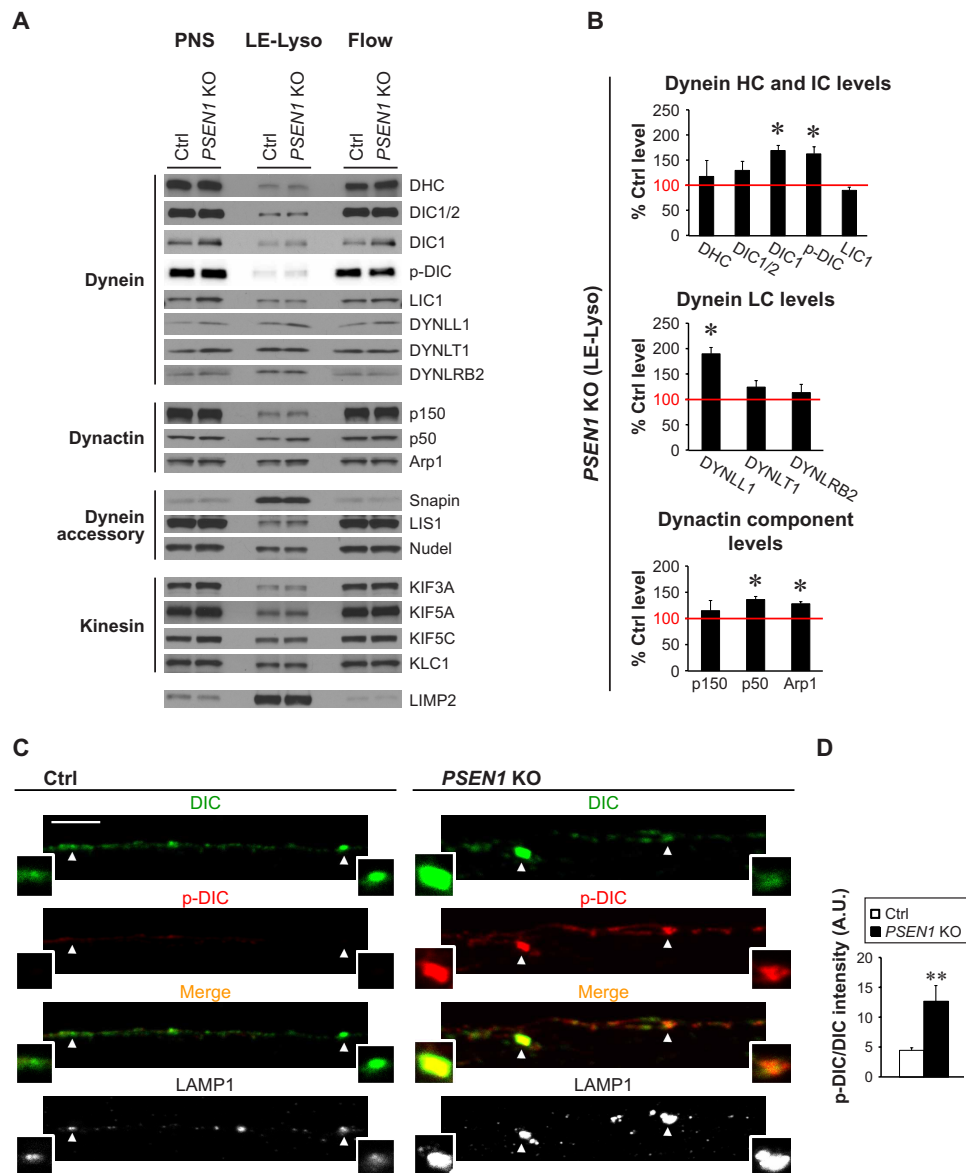


**Fig. 4. Dynein and kinesin components remain associated with LE, amphisomes, and lysosomes but DIC is hyperphosphorylated in *PSEN1* KO neurons.** (A and B) Fractionation of organelles in Ctrl and *PSEN1* KO postnuclear supernatants (PNSs) into the LE-Lyso fraction (mixture of LEs, amphisomes, and lysosomes that have taken up dextran-coated magnetite beads) and the Flow fraction (flow through containing other organelles and cytosol). (A) Representative immunoblots of dynein/dynactin components, other dynein accessory proteins, and kinesin components (see full protein names in table S1), with LIMP2 as the loading control. Eight micrograms of protein per lane. (B) Relative protein levels in the LE-Lyso fraction of *PSEN1* KO. Densitometric analysis of immunoblots in (A) followed by normalization with LIMP2 protein level. Ctrl level in each experiment is set as 100% (red line). Bars = means + SEM ( $n = 3$  to 5 experiments). \* $P < 0.05$ , Student's  $t$  test against Ctrl. HC, heavy chain; IC, intermediate chain; LC, light chain. (C and D) Immunofluorescent staining of DIC (AF633; pseudo-colored green), p-DIC-S80 (AF568; red), and LAMP1 (AF488; grayscale) in axonal segments of Ctrl and *PSEN1* KO neurons grown in microfluidics devices. Magnified images of vesicles marked by arrowheads are shown as insets. Color in merged images reflects the degree of DIC S80 phosphorylation. Scale bar, 5  $\mu$ m. (D) Graph shows LAMP1 vesicle-associated p-DIC-S80 signal intensity normalized by DIC signal intensity. A.U., arbitrary units. Bars = means + SEM ( $n = 1652$  vesicles from 64 Ctrl axons and 2662 vesicles from 95 *PSEN1* KO axons). \*\* $P < 0.01$ , Mann-Whitney  $U$  test.

To confirm the predicted role of JNK activation in disrupting LE/amphisome transport in *PSEN1* KO neurons, we performed axonal transport analysis following L-JNKi treatment (Fig. 7, A and B). Consistent with our prediction, the negative control peptide had no effects, whereas L-JNKi-mediated JNK inhibition restored the percentage of LAMP1 vesicles showing retrograde motility to near that in Ctrl neurons (Fig. 7B) and rescued the time spent pausing of LAMP1 vesicles (Fig. 7B), as well as vesicle size (Table 2). Furthermore,

restored axonal transport by L-JNKi led to reduced frequency of dystrophic neurites (Fig. 7C).

#### Aged *PSEN1*-M146V knockin mouse brains recapitulate key pathophysiological features of *PSEN1* KO neurons

To demonstrate the relevance of *PSEN1* KO model to FAD-linked *PSEN1* loss of function, we verified key findings in *PSEN1*-M146V knockin (*PSEN1* KI) mouse brains. First, we visualized the acidification

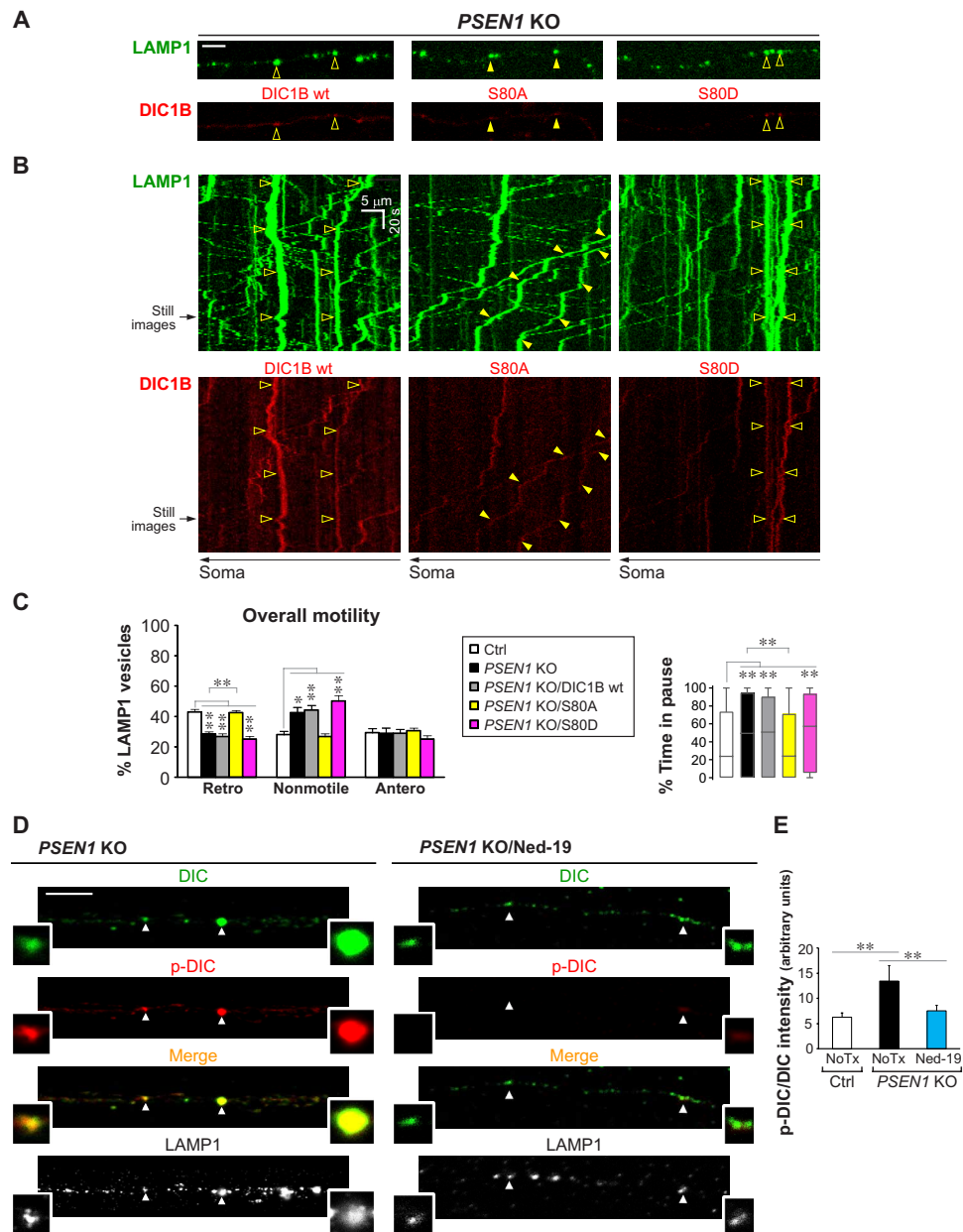


**Fig. 5. DIC hyperphosphorylation mediates defective retrograde transport of LEs/amphisomes in *PSEN1* KO neurons.** (A to C) Time-lapse imaging in Ctrl and *PSEN1* KO axons expressing LAMP1-YFP, with or without cotransfection of DIC1B-mCherry constructs (wt, wild-type; S80A, nonphosphorylatable; S80D, phosphomimetic). (A) Representative still images (left side; proximal to soma). Scale bar, 5  $\mu$ m. Closed arrowheads, retrograde; open arrowheads, nonmotile. (B) Corresponding kymographs (time = 146 s). Arrowheads show trajectories of marked vesicles in (A). (C) Quantitative analyses. Overall motility: % retrograde (retro), nonmotile (<0.1  $\mu$ m/s), and anterograde (antero) LAMP1 vesicles. Bars = means + SEM ( $n = 8, 12, 16, 19$ , and 17 axons, respectively, in Ctrl, *PSEN1* KO, *PSEN1* KO/DIC1B wt, *PSEN1* KO/S80A, and *PSEN1* KO/S80D). Percent time in pause of LAMP1 vesicles is shown by Tukey's box-and-whisker plot ( $n = 416, 637, 979, 1156$ , and 845 vesicles, respectively, in Ctrl, *PSEN1* KO, *PSEN1* KO/DIC1B wt, *PSEN1* KO/S80A, and *PSEN1* KO/S80D). (D and E) Immunofluorescent staining of DIC (AF633; pseudo-colored green), p-DIC-S80 (AF568; red), and LAMP1 (AF488; grayscale) in axonal segments of Ctrl, *PSEN1* KO, and Ned-19–treated *PSEN1* KO neurons grown in microfluidics devices. (D) Representative images of *PSEN1* KO with or without Ned-19 treatment (see also Fig. 4C). Magnified images of vesicles marked by arrowheads are shown as insets. Color in merged images reflects the degree of DIC S80 phosphorylation. Scale bar, 5  $\mu$ m. (E) Graph shows LAMP1 vesicle-associated p-DIC-S80 signal intensity normalized by DIC signal intensity. Bars = means + SEM ( $n = 706$  vesicles from 40 Ctrl axons, 2143 vesicles from 78 *PSEN1* KO axons, and 1057 vesicles from 70 *PSEN1* KO/Ned-19 axons). NoTx, untreated. (C and E) \* $P < 0.05$  and \*\* $P < 0.01$ , 1-way ANOVA with Holm-Sidak multiple comparisons or Kruskal-Wallis test with Dunn's multiple comparisons.

status of autophagy-lysosomal pathway organelles by crossing *PSEN1* KI mice with *Thy1 mRFP-eGFP-LC3 (TRGL)* mice, a transgenic reporter mouse model expressing monomeric red fluorescent protein (mRFP)–enhanced GFP (eGFP)–LC3 specifically in neurons (47).

In these mice, eGFP signal becomes quenched, whereas mRFP signal remains stable at low pH thus allowing a ratiometric estimate of changes in the acidification of AVs (47). We demonstrated autophagy-lysosomal acidification deficit in 13-month-old *PSEN1* KI mouse



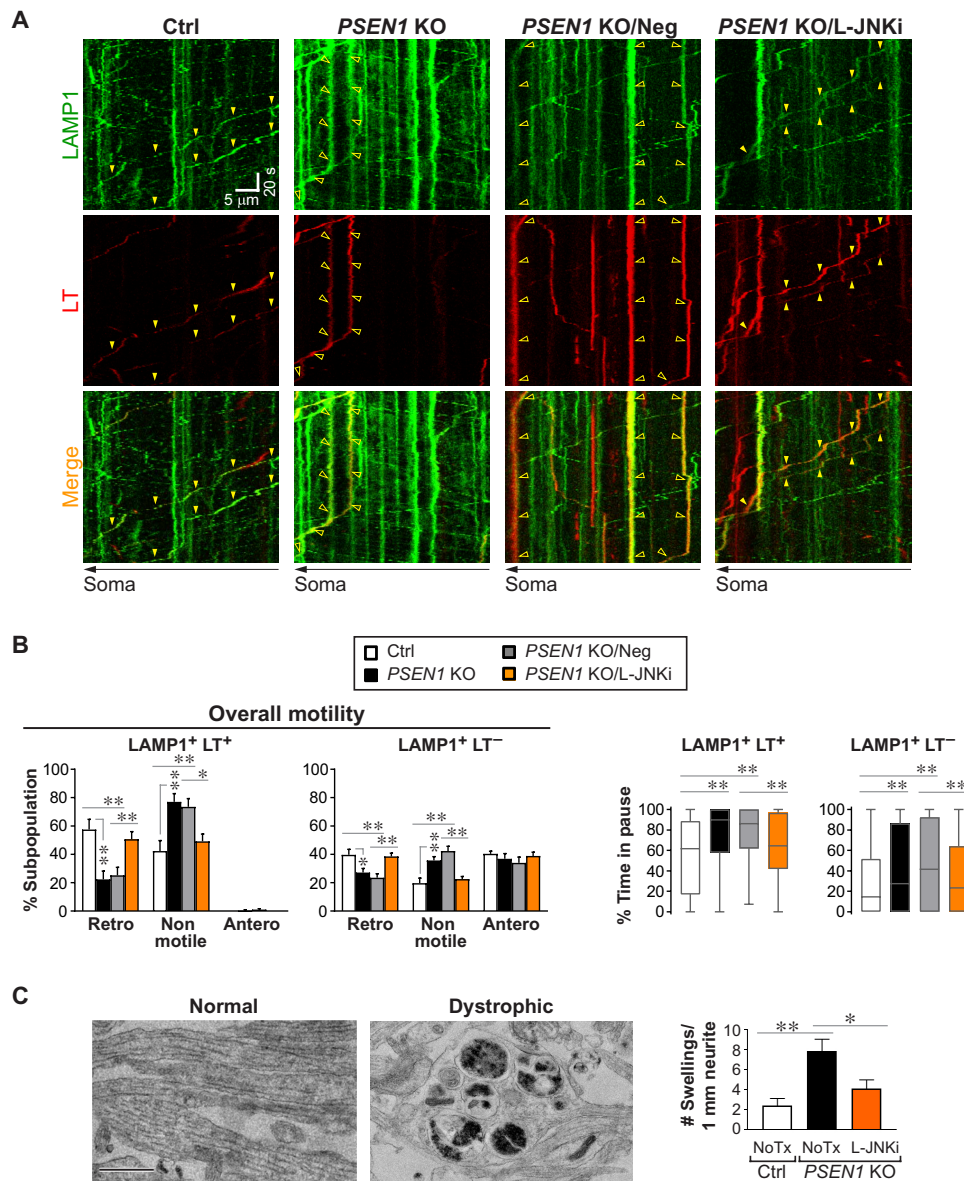


**Fig. 7. LE/amphisome retrograde transport impairment is dependent on JNK activation in *PSEN1* KO neurons.** (A and B) Time-lapse imaging in axonal segments of Ctrl and *PSEN1* KO neurons expressing LAMP1-YFP and colabeled with LT-Red. *PSEN1* KO neurons were untreated or treated with negative control peptide (Neg) or L-JNKi. (A) Representative kymographs are shown. Yellow arrowheads mark the trajectories of representative vesicles with both green (LAMP1) and red (LT) signals. Closed arrowheads, retrograde; open arrowheads, nonmotile. (B) Quantitative analyses of (A). Overall motility is represented by % retrograde (retro), nonmotile (<0.1  $\mu$ m/s), and anterograde (antero) vesicles in each LAMP1 vesicle subpopulation. Bars = means + SEM ( $n = 10, 13, 13,$  and  $14$  axons, respectively, in Ctrl, *PSEN1* KO, *PSEN1* KO/Neg, and *PSEN1* KO/L-JNKi). Percent time in pause of LAMP1 vesicles in each subpopulation is shown by Tukey's box-and-whisker plots ( $n = 72$  LT<sup>+</sup> and 418 LT<sup>-</sup> vesicles, 163 LT<sup>+</sup> and 663 LT<sup>-</sup> vesicles, 147 LT<sup>+</sup> and 577 LT<sup>-</sup> vesicles, and 148 LT<sup>+</sup> and 657 LT<sup>-</sup> vesicles respectively, in Ctrl, *PSEN1* KO, *PSEN1* KO/Neg, and *PSEN1* KO/L-JNKi). \* $P < 0.05$  and \*\* $P < 0.01$ , one-way ANOVA with Holm-Sidak multiple comparisons or Kruskal-Wallis test with Dunn's multiple comparisons. (C) Morphometric analysis of neurites in Ctrl and untreated (NoTx) or L-JNKi-treated *PSEN1* KO neurons by electron microscopy. Representative images of normal and dystrophic neurites. Scale bar, 1  $\mu$ m. Graph shows number of dystrophic swellings per 1 mm of neurites analyzed. Bars = means + SEM ( $n = 51$  to 59 images per group, Ctrl and untreated *PSEN1* KO data also used in Fig. 1D). \* $P < 0.05$  and \*\* $P < 0.01$ , Kruskal-Wallis test with Dunn's multiple comparisons.

brains by a significant increase in mRFP<sup>+</sup> eGFP<sup>+</sup> compartments (Fig. 8A). This effect was not detected in younger mice (not shown). Further aging of *PSEN1* KI mice (22 or 30 months old) resulted in formation of dystrophic neurites that contained accumulated degradative organelles (Fig. 8B) and were also enriched in p-DIC and p-JNK (Fig. 8, C and D). However, cultured neurons from embryonic *PSEN1* KI mice did not show axonal transport deficits of LE/

amphisomes (fig. S7) as in neurons with complete loss of *PSEN1* function (Fig. 1), demonstrating that a protracted aging process in vivo is necessary for axonal pathology to manifest under partial *PSEN1* loss of function. Such a protracted duration of aging possible in vivo is not achievable in vitro in cultures of primary neurons, accounting for the relatively weak phenotype of cultured *PSEN1* KI neurons versus *PSEN1* KO neurons.

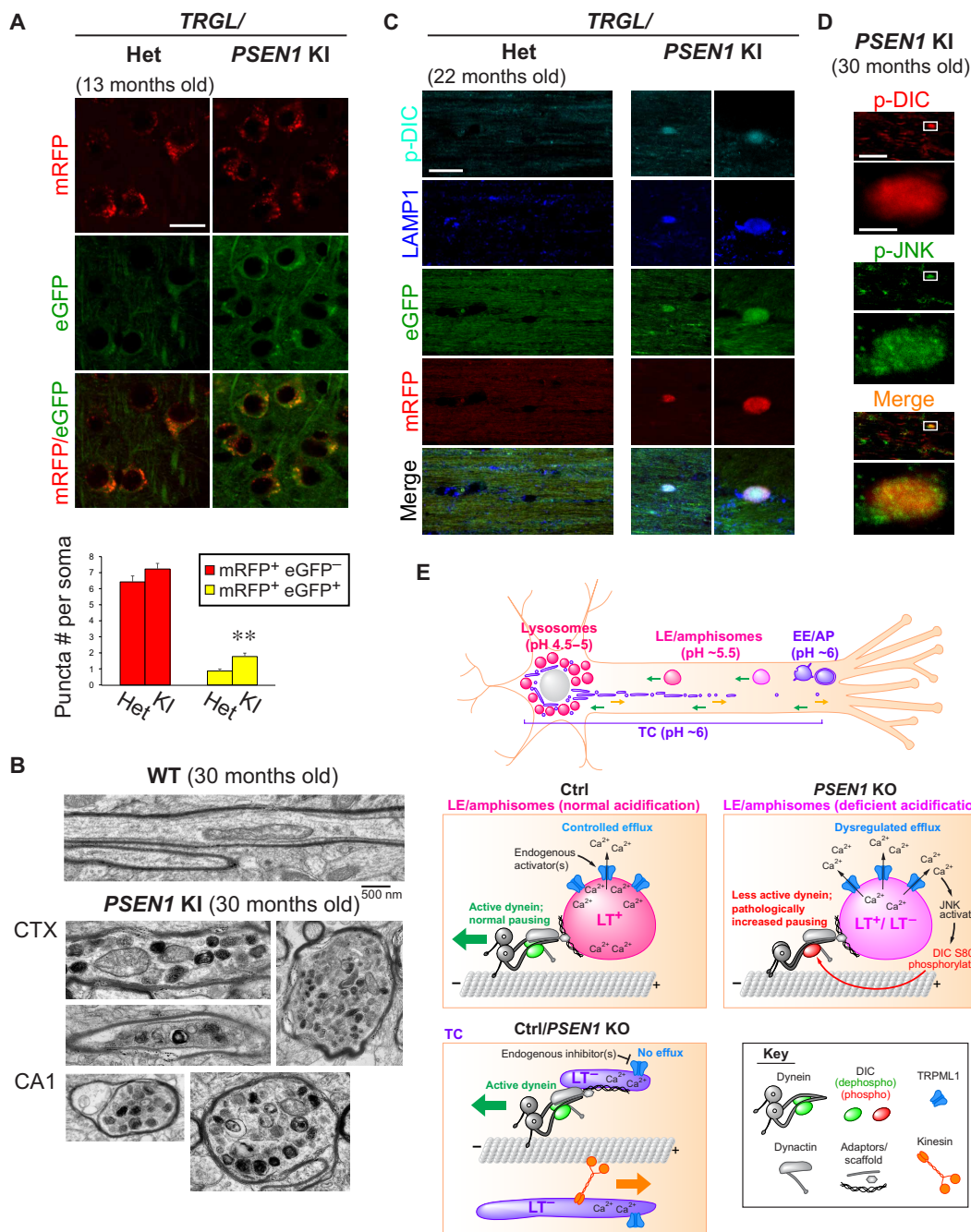


**Fig. 8. Key axonal transport pathophysiology in *PSEN1* KO neurons is recapitulated in brains of aged *PSEN1*-M146V KI mice modeling familial AD.** (A) Images of eGFP-mRFP-LC3 signal in heterozygous (het) versus homozygous *PSEN1* KI/TRGL mouse brain cortex (13 months old). Graph shows numbers of robustly acidified (mRFP<sup>+</sup> eGFP<sup>-</sup>) and poorly acidified (mRFP<sup>+</sup> eGFP<sup>+</sup>) compartments. Bars = means + SEM ( $n = 234$  and  $254$  somas in het and *PSEN1* KI).  $**P < 0.01$ , Student's  $t$  test. (B) Representative images of normal and dystrophic myelinated axons in 30-month-old wild-type (WT) and *PSEN1* KI mouse brains. CTX, brain cortex; CA1, hippocampus CA1 region. (C) Coimmunostaining of p-DIC-S80 (pseudo-colored cyan) and LAMP1 (pseudo-colored blue) in corpus callosum of heterozygous versus homozygous *PSEN1* KI/TRGL mouse brains (22 months old). (D) Coimmunostaining of p-DIC-S80 and p-JNK in corpus callosum of 30-month-old *PSEN1* KI mouse brains. (E) Hypothetical model of physiological and pathological TRPML1-mediated regulation of LAMP1 vesicle axonal transport. Top overview image shows LAMP1 vesicle subpopulations with distinct acidification, distribution, and axonal transport behaviors. Green arrows, retrograde; orange arrow, anterograde. Immature early endosomes (EEs) and autophagosomes (APs) in distal axon mature into LEs/amphisomes that undergo continuous maturation and retrograde transport in midproximal axon, with fully acidic lysosomes restricted to soma. TGN-derived TCs undergo bidirectional transport. Middle: Axonal LEs/amphisomes are largely LAMP1<sup>+</sup> LT<sup>+</sup> in both Ctrl and *PSEN1* KO, but some become insufficiently acidified (LT<sup>-</sup>) in *PSEN1* KO. In Ctrl, despite high enrichment of TRPML1 on axonal LEs/amphisomes, the acidic lumen maintains low basal TRPML1 activity. Controlled Ca<sup>2+</sup> efflux induced by endogenous agonists facilitates normal vesicle pausing. In *PSEN1* KO, acidification failure in LEs/amphisomes causes dysregulated Ca<sup>2+</sup> efflux, leading to JNK activation, DIC hyperphosphorylation, and impaired dynein activity characterized by excess pausing. Bottom: TRPML1 is inactive on highly motile TCs (LT<sup>-</sup>).

## DISCUSSION

Axonal transport is commonly disrupted in neurodegenerative diseases via unclear mechanisms. In many cases, on the basis of disease models, transport disruption is thought to be global and to involve microtubule disassembly and/or accumulation of many types of transported cargoes (48, 49). By contrast, AD and various primary lysosomal disorders are characterized by the selective accumulation of AVs and other degradative organelles containing undigested substrates in dystrophic neurites (49). Considerable evidence links various anomalies of the intraluminal environment of degradative organelles to disruption of their transport and neuritic dystrophy, but the mechanism of dystrophy formation remained undefined. We observed in our earlier study that pharmacological inhibition of lysosomal acidification disrupted AV retrograde axonal transport (7), which was subsequently confirmed by others (50). We have now defined an inside-out signaling mechanism that selectively modulates retrograde transport of LEs/amphisomes and becomes dysregulated when they fail to acidify properly, and this underlies axonal dystrophy in AD and likely other neurodegenerative diseases involving acidification deficit and  $\text{Ca}^{2+}$  dysregulation in lysosomal pathways.

### TRPML1-mediated $\text{Ca}^{2+}$ efflux selectively modulates dynein-mediated axonal transport of degradative organelles

Our hypothesis is summarized in Fig. 8E. As LEs/amphisomes mature toward lysosomal identity under normal conditions, TRPML1 progressively accumulates to a high level, but its basal activity in the absence of agonists remains low because of the highly acidic lumen (16). This enables tight control of TRPML1 activation on these organelles by endogenous agonist(s), such as phosphatidylinositol 3,5-bisphosphate (51), a low abundance signaling lipid enriched on LE membranes (39). External stimuli from the cytosol (e.g., signals triggering lipid conversion into phosphatidylinositol 3,5-bisphosphate) can induce the timely opening of TRPML1, which has a high conductance at acidic pH once it is open (52). This results in strong but temporally and spatially controlled  $\text{Ca}^{2+}$  efflux from robustly acidified organelles as needed for specific events (Fig. 8E). These events may include vesicle pausing and fusion suggested by the observed increase in LAMP1 vesicle size induced by activating TRPML1. However, in *PSEN1* KO neurons, acidification deficit in LEs/amphisomes induces an agonist-independent, inside-out activation of TRPML1 (16, 30) possibly by increasing its open probability despite an absence of agonists (52), resulting in persistent, dysregulated  $\text{Ca}^{2+}$  efflux. This leads to aberrant JNK-mediated DIC phosphorylation, which slows the dynein-mediated retrograde transport of dysfunctional degradative organelles (Fig. 8E). Unlike LEs/amphisomes, TGN-derived TCs are functionally distinct nondegradative biosynthetic carriers of lysosomal proteins, and their motility is only mildly affected by *PSEN1* KO (Fig. 8E). This is likely because they lack compatible membrane lipids such as phosphatidylinositol 3,5-bisphosphate (38), which may act as a permissive cofactor required for TRPML1 activation (40) in addition to its role as an agonist (51).

Supporting the scenario in Fig. 8E, we could rescue transport impairment by intervening at any of multiple levels in this mechanism, which concurrently normalized pathological vesicle enlargement and reversed neuritic dystrophy. Rescue effects from these molecular interventions were able to override the effect of the acidification deficit in *PSEN1* KO neurons. We have shown that vesicle enlargement contributed to increased total LAMP1 vesicle volume

in the axoplasm. After only weeks of perturbed trafficking in these cultured neurons with complete loss of *PSEN1* function, the increased burden of cargo and mild dystrophic swellings seen at this early stage are likely preconditions for the extensive dystrophy in aged human AD brains after decades of perturbation *in vivo* (53). These early dystrophic changes in our study were eliminated by correcting the transport deficit via Ned-19 inhibition of  $\text{Ca}^{2+}$  efflux. It is noted that under partial *PSEN1* loss of function, as in *PSEN1* KI mice, transport deficits and neuritic dystrophy only start to manifest after at least 1 year of aging *in vivo*. The mechanism we advance here for LE/amphisome retrograde transport impairment induced by familial AD-linked acidification deficit and TRPML1 dysregulation is also likely relevant more generally to pathogenesis of other neurodegenerative diseases involving lysosomal pathway dysfunction (54). The link between TRPML1 activity and acidification is also relevant to mild cases of mucopolidosis type IV, which are caused by TRPML1 mutants that become unresponsive to the sharp inhibition of spontaneous channel activity by low luminal pH (30). Furthermore, deacidification-induced hyperactivity is potentially a general phenomenon in the TRPML subfamily, since TRPML3 is also activated by high pH as a mechanism for inducing exocytosis upon sensing lysosome neutralization by pathogens (55).

In apparent conflict with our results, proper TRPML1 channel activity was shown to be necessary for starvation-induced retrograde transport of LAMP1 vesicles in non-neural cells (56). In this case, however, TRPML1 is activated via physiological signaling under strict spatial and temporal regulation, in contrast to the uncontrolled pathological TRPML1 activity in *PSEN1* KO or ML-SA1-treated Ctrl neurons. Depending on the magnitude and duration of  $\text{Ca}^{2+}$  efflux, as well as cell type and stimuli involved, TRPML1 activity conceivably activates different sets of downstream effectors that produce distinctive responses. For instance, DIC S80 phosphorylation is required for its recruitment on endosomes (13), and thus, transient TRPML1 activation and DIC S80 phosphorylation may well be beneficial for dynein recruitment. However, on the basis of our observations that prolonged and dysregulated TRPML1 hyperactivity and DIC hyperphosphorylation are both detrimental to LE/amphisome retrograde transport, we envision that TRPML1 is inactivated after dynein recruitment, and that DIC is dephosphorylated for its processive retrograde movement. We showed that pathological TRPML1 hyperactivity abnormally activated kinases, impaired motor activity, and even caused lysosomal deacidification under our experimental conditions, contradicting the acidifying effect of very short ML-SA1 treatments in some studies (34, 36). For this reason, the development of TRPML1 agonists as therapies for diseases implicating TRPML1 deficiency should proceed with caution.

### Loss of retrograde motility of degradative organelles in *PSEN1* KO neurons is a result of impaired dynein activity due to DIC hyperphosphorylation

In our measurements of motor components and accessory proteins associated with the LE-Lyso fraction consisting of LEs, amphisomes, and lysosomes, we could not detect a reduction in levels of examined motor proteins in *PSEN1* KO neurons compared to controls. Given this observation, the loss of LE/amphisome retrograde motility was more likely due to an impaired activity of dynein residing on these organelles, but not the failure in dynein recruitment. Supporting this idea, we showed a significantly higher level of DIC

S80 phosphorylation in axonal LAMP1 vesicles of *PSEN1* KO neurons than in Ctrl and that expression of a nonphosphorylatable DIC1B-S80A mutant, but not wild-type DIC1B or phosphomimetic DIC1B-S80D, fully restored the transport deficit of LAMP1 vesicles. Processive dynein movement and force production involves its coordination with various accessory proteins, such as dynactin (10) and NudE-like (Nudel) (57). Notably, DIC binding to dynactin p150 subunit or Nudel was reported to be negatively regulated by the phosphorylation of several closely located residues in the DIC serine-rich region (11, 12, 58), which also harbors our site of interest. Supporting this concept, a recent structural study demonstrated that a conformational change in p-DIC blocked the access of p150 (59). Further studies are needed to clarify the effects of phosphorylation status of multiple residues on dynein structure and function.

### DIC hyperphosphorylation in *PSEN1* loss of function is mediated by excess JNK activity

JNK is one of the kinases predicted to phosphorylate DIC S80 (45), susceptible to  $Ca^{2+}$ -mediated activation (43), and abnormally active in *PSEN1*-deficient cells (60), as we also show. Furthermore, JNK inhibition blocked DIC hyperphosphorylation, restored LE/amphisome retrograde transport, and decreased neuritic dystrophy in *PSEN1* KO neurons, demonstrating that the hyperactivity of JNK, and possibly additional  $Ca^{2+}$ -activated kinases, contributes to the impaired dynein-mediated transport in *PSEN1* KO neurons. Signals that regulate JNK activity are coordinated in part by JNK-interacting proteins (JIPs), which serve as scaffolds that facilitate interaction of JNK with its activators and inhibitors (61, 62). Given that JIPs are required for normal transport behavior of degradative organelles in axons (63–65), it will be of interest to examine their potential roles, if any, in the mechanism defined here. Complementary to kinases, phosphatases are also important regulators of dynein-mediated transport. For instance, inhibition of protein phosphatase 1 (PP1) and/or PP2A activity in neurons impaired dynein-mediated transport of specific cargoes (66, 67), including AVs (68), and induced neuritic swellings (69).

### Perspectives

In support of our hypothesis, previous studies have shown direct or indirect association of TRPML1 (70), JNK (71), and dynactin (56) with apoptosis-linked gene 2, a calcium-binding protein, suggesting the presence of these proteins in a macromolecular complex that mediates the pathological signaling proposed in the present study. Coupled with the impaired substrate degradation due to reduced acid hydrolase activity (15), inefficient transport of vesicles in the lysosomal system shown here leads to vesicle accumulation and axonopathy. Our findings provide a framework for future investigations of this mechanism in a widening range of neurodegenerative diseases recently recognized to involve acidification failure in lysosomal pathways (54).

## MATERIALS AND METHODS

### Experimental design

Dysregulation of calcium signaling in lysosomal pathway organelles in axons was interrogated in cultured mouse neurons by two approaches. The first approach was directly manipulating TRPML1-mediated  $Ca^{2+}$  efflux in neurons with small-molecule TRPML1 agonist or inhibitor. The second approach was using neurons isolated from *PSEN1* KO mouse embryos. The *PSEN1* KO model is known to show TRPML1 hyperactivity induced by lysosomal acidification deficit (16).

Using these approaches, effects of abnormal  $Ca^{2+}$  efflux were systematically studied in lysosomal pathway organelles in terms of their axonal transport behavior, dimensions, presence in neuritic dystrophy, associated motor protein levels, and phosphorylation status. The pathological mechanism was investigated with rescues at multiple levels of the hypothesized pathway. Key pathological features of *PSEN1* KO neurons were verified in FAD-linked *PSEN1-M146V* KI mice.

### Antibodies, plasmids, and primers

Commercially available antibodies used are summarized in table S1. A rabbit polyclonal antibody against p-DIC was custom-made by Biomatik Corporation using the peptide sequence CVPTPM(pS) PSSKSVST. This antibody targets p-S80 of mouse DIC1B and the corresponding residue in other mouse DIC isoforms. Specificity of this antibody against the phosphorylated epitope was confirmed by peptide competition assay (fig. S5).

LAMP1-YFP plasmid was a gift from J. Swanson, University of Michigan, Ann Arbor, MI, USA. LAMP1-mCherry plasmid was constructed by subcloning the LAMP1 fragment from LAMP1-YFP in-frame into pmCherry-N1 vector (Clontech). LC3-RFP-GFP was a gift from T. Yoshimori, Osaka University, Japan (72). Rab7-DsRed was purchased from Addgene (73). Rab7-GFP was a gift from A. Cataldo. LAMP1-GCaMP plasmid was constructed by substituting the TPC2 fragment in pGCaMP6m-N3-TPC2 (Addgene) (74) with LAMP1 fragment. SureSilencing shRNA against TRPML1 (mouse MCOLN1, clone 2) and negative control plasmids with GFP were purchased from QIAGEN, as described (16). pDsRed2-Mito was purchased from Clontech.

Plasmids for expressing DIC1B-mCherry were generated in-house. Mouse DIC1B was amplified by reverse transcription polymerase chain reaction (PCR) with the primer pair GCG TAC AGC ATT CAG GAA and AGT GAG TAG GTA CAC GTG. Restriction sites were added by nested PCR with the primer pair TCA GAT CTC AGC ATT CAG GAA GCA AAC A and CCG TCG ACT GGG CAG CTA ACT CAA CAG C. Restriction enzyme-digested DNA was cloned into the Bgl II and Sal I cloning sites of pmCherry-N1 vector (Clontech) and was transformed into XL10-Gold ultracompetent cells (Agilent). Point mutants on S80 were generated using the QuikChange II XL site-directed mutagenesis kit (Agilent) with mutagenic primer pairs (for DIC1B-S80A: GTC CCA ACC CCT ATG GCT CCC TCT TCG AAA TC and GAT TTC GAA GAG GGA GCC ATA GGG GTT GGG AC; for DIC1B-S80D: GTC CCA ACC CCT ATG GAT CCC TCT TCG AAA T and ATT TCG AAG AGG GAT CCA TAG GGG TTG GGA C). Flag-tagged DIC1B constructs were generated by replacing the mCherry sequence with an annealed DNA fragment containing Flag-tag sequence flanked by restriction sites: CCG GTC GGA TCC GAT TAC AAG GAT GAC GAC GAT AAG TAA GC and GGC CGC TTA CTT ATC GTC GTC ATC CTT GTA ATC GGA TCC GA. Accuracy of the coding sequences was verified by DNA sequencing.

### Animals and primary neuronal culture

Animal use was approved by the Institutional Animal Care and Use Committee at the Nathan Kline Institute. *PSEN1-M146V* KI mice (*PSEN1* KI) was a gift from M. Mattson. *PSEN1* KI/*TRGL* mice were generated by crossing *PSEN1* KI and *TRGL* (*Thy1 mRFP-eGFP-LC3*, line 6) transgenic mice (47). Primary cortical neurons were isolated on the basis of the procedures described in (75) from E16 (embryonic day 16) to E17 mouse embryos, which were derived

from crossing *PSEN1*<sup>+/-</sup> mice, or homozygous *PSEN1* KI mice, or wild-type mice maintained in C57BL/6 background. For Ctrl neurons, both wild-type (*PSEN1*<sup>+/+</sup>) and heterozygous (*PSEN1*<sup>+/-</sup>) siblings were used, as previously described (76). This approach was beneficial because stress on neurons during the isolation process was reduced in the streamlined procedure. Heterozygous neurons, which retained 50% of functional PSEN1, were capable of maintaining normal LAMP1 vesicle axonal transport comparable to that of wild-type neurons in our preliminary experiments. Cerebral cortices were dissected on ice and incubated in enzyme solution [Hibernate E medium (Brainbits) containing papain (10 U/ml; Worthington Biochemical) and deoxyribonuclease I (DNase I) (0.2 mg/ml; Sigma-Aldrich)] at 37°C for 15 min. The reaction was mixed with an equal volume of Hibernate E containing 10% fetal bovine serum (FBS) and centrifuged at 1000 rpm for 5 min. Digested cortices were resuspended in plating medium A [Dulbecco's modified Eagle's medium/F-12 and GlutaMAX supplement (Thermo Fisher Scientific) containing 5% horse serum and 5% FBS]. After removal of debris with a 40- $\mu$ m nylon filter, neurons suspended in plating medium A were plated on poly-D-lysine-coated culture dishes or glass coverslips unless otherwise specified. For live imaging, neurons were plated at  $0.24 \times 10^6$  cells/cm<sup>2</sup> on glass bottom dishes with 14-mm microwells (Cellvis). For feeder neuron cultures and subcellular fractionation, neurons were plated at  $0.3 \times 10^6$  to  $0.45 \times 10^6$  cells/cm<sup>2</sup> on culture dishes. For electron microscopy, neurons were plated at  $0.45 \times 10^6$  cells/cm<sup>2</sup> on glass coverslips. For pH measurement, neurons were plated at  $0.2 \times 10^6$  cells/cm<sup>2</sup> on 96-well plates. Plating medium A was replaced with culture medium [Neurobasal medium supplemented with B27 and GlutaMAX (Thermo Fisher Scientific)] 1.5 hours after plating. Alternatively, for immunofluorescent staining and Ca<sup>2+</sup> imaging experiments, neurons were cultured in microfluidics device with 450- $\mu$ m microgrooves (Xona). Before plating, microfluidics devices were pretreated with pentane, xylenes, ethanol, and sterile water (77), were subsequently dried and sterilized under ultraviolet for 10 min, were bonded to poly-D-lysine-coated glass bottom dishes with 30-mm microwells (Cellvis), and were prewetted with plating medium B (Neurobasal medium containing 10% FBS). Neurons were pelleted and resuspended to a concentration of  $5 \times 10^6$  cells/ml in plating medium B, with 15  $\mu$ l of cell suspension added to the somal channel of each microfluidics. This resulted in a low cell density that helped preventing multiple axons from growing through the same microgroove. Plating medium B was added to fill up the somal wells and half-fill the axonal wells after 40 min and was replaced with conditioned culture medium from feeder neuron cultures after 24 hours. Neurons were maintained for 5 to 10 days in vitro (DIV) at 37°C in 95% air and 5% CO<sub>2</sub> with half of the culture medium being replaced every 3 days.

### Transfection and treatments of cultured neurons

Neurons were transfected on 3 to 5 DIV with endotoxin-free plasmids for the expression of fluorescently tagged fusion proteins or shRNAs using Lipofectamine 2000 (Thermo Fisher Scientific) according to the manufacturer's instructions with modifications. Each transfection mix was prepared in Opti-MEM (Thermo Fisher Scientific) containing 0.368  $\mu$ g of DNA and 1.05  $\mu$ l of Lipofectamine (for single plasmid transfection), or 0.375  $\mu$ g of DNA and 0.625  $\mu$ l of Lipofectamine (for cotransfection of two plasmids). After incubation with transfection mix for 50 min or 24 hours for single and cotransfection, respectively, neurons were washed in Neurobasal medium, fed with

culture medium described above (50% conditioned and 50% fresh), and imaged 2 to 3 days after start of transfection. Efficacy of shRNA-mediated TRPML1 knockdown has been shown previously (16).

Neurons were treated with the following reagents diluted with culture medium (at least 50% conditioned) at specified concentrations and durations: Ned-19 (Enzo Life Sciences), 0.4  $\mu$ M for 16 hours; ML-SA1 (EMD Millipore), 100  $\mu$ M for 22 min (exception: 2-hour treatment for electron microscopy); L-JNKi or negative control peptide (EMD Millipore), 1  $\mu$ M for 24 hours; LT-Red (Thermo Fisher Scientific), 0.25  $\mu$ M for 22 min; Bodipy FL-Pepstatin A (Thermo Fisher Scientific), 0.96  $\mu$ M for 30 min; and dextran-OG488 and dextran-AF647, each at 0.1 mg/ml for 16 hours. For cytosolic Ca<sup>2+</sup> imaging, neurons cultured in microfluidics devices were incubated with 5  $\mu$ M OG488 Bapta-1 AM (Thermo Fisher Scientific) diluted in imaging medium [Hibernate E-low fluorescence (Brainbits) supplemented with B27 and GlutaMAX] for 20 min at room temperature, followed by a 10-min wash in fresh imaging medium at room temperature. For mitochondrial Ca<sup>2+</sup> imaging, neurons were incubated with both 0.5  $\mu$ M Rhod-2 AM (Thermo Fisher Scientific) and 0.5  $\mu$ M MitoTracker green (Thermo Fisher Scientific) diluted in imaging medium for 30 min at room temperature, followed by washes in fresh imaging medium.

### Live cell imaging

Neurons were washed and maintained in the imaging medium described above. Live imaging was performed at 37°C except for cytosolic Ca<sup>2+</sup> imaging and mitochondrial Ca<sup>2+</sup> imaging, which were performed at room temperature. Neurons were imaged with a Zeiss LSM 510 or a Zeiss LSM 880 laser scanning confocal microscope. Time-lapse imaging was performed in three random axonal segments (~55  $\mu$ m each) within the proximal 50 to 300  $\mu$ m region of each axon identified on the basis of the morphology of a long and untapered process. At least 200 images per channel were taken over a 3-min period. Multitrack line scanning was used for scanning more than one channel. Time-lapse series were processed with a 1-pixel median filter in ImageJ, and kymographs were constructed with the Multiple Kymograph plugin along manually traced axonal profiles. Brightness and contrast of displayed images and kymographs (shown at X scale = 1 and Y scale = 4) were adjusted in ImageJ and/or Photoshop. Unadjusted images and kymographs from at least three independent neuronal cultures were analyzed in ImageJ to measure signal intensities and vesicle motility based on the transport parameters defined below:

- 1) Average velocity (in micrometers per second): Total net displacement/total duration of the entire track. Vesicles with average velocities of <0.1  $\mu$ m/s were classified as nonmotile. Motile vesicles displaced toward the axon terminal were classified as "anterograde," and those displaced toward the cell body were classified as "retrograde." The overall motility of vesicle population was shown as percentages of anterograde, retrograde, and nonmotile vesicles.
- 2) Run: A segment within a track, during which the vesicle travels at  $\geq 0.1$   $\mu$ m/s in a single direction without interruptions.
- 3) Run time (in seconds): Duration of a given run.
- 4) Run length (in micrometers): Displacement of a given run. An average value of all runs is calculated for each vesicle.
- 5) Segmental velocity (in micrometers per second): Run length/run time of a given run. Average values of all anterograde runs and all retrograde runs are calculated for each vesicle.

- 6) Pause: A segment within a track, during which the vesicle travels at  $<0.1 \mu\text{m/s}$ .
- 7) Pause frequency (times per minute): Number of times a vesicle switches from a run to a pause divided by the total run time in the entire track.
- 8) Percent time in pause: Duration of all pauses/total duration of the entire track  $\times 100\%$ .
- 9) Switch frequency (times per second): Number of times a vesicle switches direction between runs (including switching events interrupted by a pause) divided by the total duration of all runs and pauses.

### Lysosomal pH measurement

Lysosomal pH was measured as described (78) with modifications. Neurons were pulsed on 4 DIV with LysoSensor Yellow/Blue dextran (0.3 mg/ml; Thermo Fisher Scientific) for 24 hours, followed by washes and a 16-hour chase in culture medium (50% conditioned and 50% fresh). Before fluorescence measurement, neurons were either washed with the imaging medium described above or incubated for 1.5 hours with pH calibration buffer [10  $\mu\text{M}$  monensin and 10  $\mu\text{M}$  nigericin in MES buffer (5 nM NaCl, 115 mM KCl, 1.3 mM  $\text{MgSO}_4$ , and 25 mM MES) adjusted to pH 4.0, 5.0, 5.5, 6.0, or 7.0]. Dual fluorescence emission (excitation, 355 nm; emission, 440 and 535 nm) of neurons bathed in imaging medium or pH calibration buffer was measured with a Wallac Victor 2 fluorimeter (PerkinElmer). Ratio of emission (535 nm:440 nm) was calculated for the determination of pH.

### Subcellular fractionation to obtain LE-Lyso fraction

PNSs of neurons were fractionated to obtain an organelle fraction enriched in LEs, amphisomes, and lysosomes (termed LE-Lyso fraction) as described (16, 79) with minor modifications. Neurons were pulsed with culture medium (50% conditioned and 50% fresh) containing 10% dextran-conjugated magnetite (Liquid Research LLC) and 1 mM Hepes (pH 7.4) for 24 hours, followed by washes in phosphate-buffered saline (PBS) and a 16-hour chase in normal culture medium to allow dextran accumulation in LEs/amphisomes and lysosomes. Neurons were harvested in ice-cold hypotonic buffer A [10 mM Hepes (pH 7.2), 15 mM KCl, and 1.5 mM MgAc] supplemented with protease and phosphatase inhibitors. Homogenization was performed by 30 strokes in a loose-fitting dounce homogenizer, followed by two passes in 18-gauge syringe needles and three passes in 23-gauge syringe needles. The resulting homogenates were mixed with  $\frac{1}{8}$  volume of hypertonic buffer B [220 mM Hepes (pH 7.2), 375 mM KCl, and 22.5 mM MgAc] supplemented with DNase I and then centrifuged at 1500 rpm for 10 min at 4°C to obtain the PNSs. An aliquot was collected from each PNS sample, with the remaining PNSs added to previously equilibrated QuadroMAC LS columns assembled with a magnet to capture dextran-containing compartments. Unbound PNS was added to the column again, and the resulting unbound flow-through (“Flow”) fractions were collected. The columns were then incubated with DNase I for 10 min, followed by extensive washes in PBS. Last, the columns were disassembled from the magnet to elute LE-Lyso fractions with PBS containing 5% sucrose and supplemented with protease and phosphatase inhibitors. Membranous organelles in the LE-Lyso fractions were pelleted at 21,050g for 60 min at 4°C and were resuspended in small volumes of IP (immunoprecipitation) lysis buffer [10 mM tris, 150 mM NaCl, 1 mM EDTA, 1 mM EGTA, 1% Triton X-100, and 0.5% NP-40 (pH 7.4)]

supplemented with protease and phosphatase inhibitors. Eight micrograms of proteins from all collected samples were subjected to SDS-polyacrylamide gel electrophoresis and immunoblot analysis as described (15). Data were collected from at least three independent experiments.

### Membrane preparation

Neurons were harvested in membrane prep buffer [250 mM sucrose, 5 mM tris-HCl (pH 7.4), 1 mM EGTA, and protease/phosphatase inhibitors]. Homogenization was performed by 10 passes in 26-gauge syringe needles and then incubated on ice for 10 min. The resulting homogenates were centrifuged at 1000g for 10 min at 4°C to obtain the PNSs. An aliquot was collected as a PNS sample, and the remaining PNSs were then centrifuged at 125,000g for 60 min at 4°C to pellet membrane organelles. The supernatants were collected as cytosol fractions, the pellets were washed with membrane prep-buffer (125,000g for 30 min at 4°C) and then resuspended in IP lysis buffer supplemented with protease and phosphatase inhibitors.

### Immunofluorescent staining

Neurons were harvested for immunofluorescent staining on 8 to 10 DIV. Neurons were subjected to prefixation extraction with detergent to remove soluble proteins in the cytosol by incubating in 0.02% saponin in Pipes buffer [80 mM Pipes (pH 6.9), containing 1 mM EGTA, 3 mM  $\text{MgCl}_2$ , and 30% glycerol] on ice for 1 min (80), followed by two washes in Pipes buffer without detergent and fixation in 4% paraformaldehyde in Pipes buffer for 20 min at room temperature. Thereafter, neurons were washed three times in PBS, followed by permeabilization in 0.02% Triton X-100/tris-buffered saline (TBS) (pH 7.4), for 10 min, and three washes in TBS. Neurons were then subjected to the following incubations at room temperature: 10% normal goat serum/TBS for 1.5 hours; primary antibodies diluted in 1% bovine serum albumin (BSA)/TBS overnight at 4°C; three washes in TBS; AF secondary antibodies diluted in 1% BSA/TBS for 40 min; and three washes in TBS. Neurons were mounted in Fluoro Gel with tris buffer (Electron Microscopy Sciences). Random segments of proximal-mid axons (proximal 225- $\mu\text{m}$  region within microgrooves) were imaged by laser scanning confocal microscopy (multitrack line scanning) using Zeiss LSM 510 or Zeiss LSM 880 confocal microscope. Only axons that had extended beyond microgrooves into the axonal chamber were selected for imaging. Immunostaining of brain sections was performed as described (9). Brightness and contrast of displayed images were adjusted in ImageJ and/or Photoshop. Unadjusted images were analyzed in ImageJ with particle analysis or line scan. Data were collected from at least three independent experiments.

### Electron microscopy

Electron microscopy was performed as described (7, 9). For cultured neurons, DIV 6 to 7 neurons were washed in fresh culture medium and fixed in 4% paraformaldehyde/1% glutaraldehyde/5% sucrose in 0.1 M sodium cacodylate (pH 7.2) (Electron Microscopy Sciences) for 24 hours at room temperature. For mouse brains, mice were perfused with 4% paraformaldehyde/2% glutaraldehyde in 0.1 M sodium cacodylate buffer (pH 7.4), followed by immersion fixation of mouse brains in the same fixative overnight. Fixed neurons or vibratome brain sections were then washed and postfixed in 1% osmium tetroxide, dehydrated in a graded series ethanols (50 to 100%), and embedded in Epon or Spurr Resin (Electron Microscopy Sciences) for at least

3 days. Ultrathin sections of 60 nm in thickness were obtained by cutting in parallel to the plane of culture substratum, followed by staining with uranyl acetate and lead citrate. For each sample from three independent cultures, low magnification (3400 to 7900 $\times$  direct magnification) electron micrographs were randomly captured from neurite-enriched fields containing 1 to 2 mm of neurites in total. High-magnification images (8500 to 25,000 $\times$ ) were acquired in areas containing neuritic dystrophies, defined as organelle-filled swellings with a diameter of at least 1  $\mu$ m. Images were analyzed to quantify the frequency and contents of dystrophic swellings.

### Statistical analysis

All data were pooled from at least three independent neuronal cultures and sample sizes were specified in figure legends. Statistical analysis was performed in either GraphPad Prism 8.0.1 or IBM SPSS Statistics 24. Normality of data distribution was tested with Shapiro-Wilk test. For normally distributed data, unpaired two-tailed Student's *t* test (equal variance not assumed) was used for comparing two groups, and one-way analysis of variance (ANOVA) followed by multiple comparisons was used for comparing three or more groups. For non-normally distributed data, nonparametric tests or Welch's ANOVA were performed. Unpaired two-tailed Mann-Whitney *U* test was used to compare two groups, and Welch's ANOVA or Kruskal-Wallis test followed by multiple comparisons was used for comparing three or more groups. Source data are provided in data S1.

### SUPPLEMENTARY MATERIALS

Supplementary material for this article is available at <https://science.org/doi/10.1126/sciadv.abj5716>

[View/request a protocol for this paper from Bio-protocol.](#)

### REFERENCES AND NOTES

- S. E. Encalada, L. S. Goldstein, Biophysical challenges to axonal transport: Motor-cargo deficiencies and neurodegeneration. *Annu. Rev. Biophys.* **43**, 141–169 (2014).
- S. Maday, A. E. Twelvetrees, A. J. Moughamian, E. L. Holzbaur, Axonal transport: Cargo-specific mechanisms of motility and regulation. *Neuron* **84**, 292–309 (2014).
- B. Ravikumar, A. Acevedo-Arozena, S. Imarisio, Z. Berger, C. Vacher, C. J. O'Kane, S. D. Brown, D. C. Rubinsztein, Dynein mutations impair autophagic clearance of aggregate-prone proteins. *Nat. Genet.* **37**, 771–776 (2005).
- R. A. Nixon, in *Lysosomes: Biology, Diseases, and Therapeutics*, F. R. Maxfield, J. M. Willard, S. Lu, Eds. (John Wiley & Sons Inc., 2016), chap. 9.
- P. P. Y. Lie, R. A. Nixon, Lysosome trafficking and signaling in health and neurodegenerative diseases. *Neurobiol. Dis.* **122**, 94–105 (2019).
- X. T. Cheng, B. Zhou, M. Y. Lin, Q. Cai, Z. H. Sheng, Axonal autophagosomes use the ride-on service for retrograde transport toward the soma. *Autophagy* **11**, 1434–1436 (2015).
- S. Lee, Y. Sato, R. A. Nixon, Lysosomal proteolysis inhibition selectively disrupts axonal transport of degradative organelles and causes an Alzheimer's-like axonal dystrophy. *J. Neurosci.* **31**, 7817–7830 (2011).
- S. Maday, K. E. Wallace, E. L. Holzbaur, Autophagosomes initiate distally and mature during transport toward the cell soma in primary neurons. *J. Cell Biol.* **196**, 407–417 (2012).
- P. P. Y. Lie, D. S. Yang, P. Stavrides, C. N. Goulbourne, P. Zheng, P. S. Mohan, A. M. Cataldo, R. A. Nixon, Post-Golgi carriers, not lysosomes, confer lysosomal properties to pre-degradative organelles in normal and dystrophic axons. *Cell Rep.* **35**, 109034 (2021).
- R. J. McKenney, W. Huynh, M. E. Tanenbaum, G. Bhabha, R. D. Vale, Activation of cytoplasmic dynein motility by dynactin-cargo adapter complexes. *Science* **345**, 337–341 (2014).
- F. J. Gao, S. Hebbbar, X. A. Gao, M. Alexander, J. P. Pandey, M. D. Walla, W. E. Cotham, S. J. King, D. S. Smith, GSK-3 $\beta$  phosphorylation of cytoplasmic dynein reduces Ndel1 binding to intermediate chains and alters dynein motility. *Traffic* **16**, 941–961 (2015).
- J. Whyte, J. R. Bader, S. B. Tauhata, M. Raycroft, J. Hornick, K. K. Pfister, W. S. Lane, G. K. Chan, E. H. Hinchcliffe, P. S. Vaughan, K. T. Vaughan, Phosphorylation regulates targeting of cytoplasmic dynein to kinetochores during mitosis. *J. Cell Biol.* **183**, 819–834 (2008).
- D. J. Mitchell, K. R. Blasier, E. D. Jeffery, M. W. Ross, A. K. Pullikuth, D. Suo, J. Park, W. R. Smiley, K. W. Lo, J. Shabanowitz, C. D. Deppmann, J. C. Trinidad, D. F. Hunt, A. D. Catling, K. K. Pfister, Trk activation of the ERK1/2 kinase pathway stimulates intermediate chain phosphorylation and recruits cytoplasmic dynein to signaling endosomes for retrograde axonal transport. *J. Neurosci.* **32**, 15495–15510 (2012).
- J. Scherer, J. Yi, R. B. Vallee, PKA-dependent dynein switching from lysosomes to adenovirus: A novel form of host-virus competition. *J. Cell Biol.* **205**, 163–177 (2014).
- J. H. Lee, W. H. Yu, A. Kumar, S. Lee, P. S. Mohan, C. M. Peterhoff, D. M. Wolfe, M. Martinez-Vicente, A. C. Massey, G. Sovak, Y. Uchiyama, D. Westaway, A. M. Cuervo, R. A. Nixon, Lysosomal proteolysis and autophagy require presenilin 1 and are disrupted by Alzheimer-related PS1 mutations. *Cell* **141**, 1146–1158 (2010).
- J. H. Lee, M. K. McBrayer, D. M. Wolfe, L. J. Haslett, A. Kumar, Y. Sato, P. P. Lie, P. Mohan, E. E. Coffey, U. Kompella, C. H. Mitchell, E. Lloyd-Evans, R. A. Nixon, Presenilin 1 maintains lysosomal Ca<sup>2+</sup> homeostasis via TRPML1 by regulating vATPase-mediated lysosome acidification. *Cell Rep.* **12**, 1430–1444 (2015).
- L. Sun, R. Zhou, G. Yang, Y. Shi, Analysis of 138 pathogenic mutations in presenilin-1 on the in vitro production of A $\beta$ 42 and A $\beta$ 40 peptides by  $\gamma$ -secretase. *Proc. Natl. Acad. Sci. U.S.A.* **114**, E476–E485 (2017).
- B. De Strooper, Loss-of-function presenilin mutations in Alzheimer disease. Talking point on the role of presenilin mutations in Alzheimer disease. *EMBO Rep.* **8**, 141–146 (2007).
- K. Coen, R. S. Flannagan, S. Baron, L. R. Carraro-Lacroix, D. Wang, W. Vermeire, C. Michiels, S. Munck, V. Baert, S. Sugita, F. Wuytack, P. R. Hiesinger, S. Grinstein, W. Annaert, Lysosomal calcium homeostasis defects, not proton pump defects, cause endo-lysosomal dysfunction in PSEN-deficient cells. *J. Cell Biol.* **198**, 23–35 (2012).
- H. Tu, O. Nelson, A. Bezprozvanny, Z. Wang, S. F. Lee, Y. H. Hao, L. Serneels, B. De Strooper, G. Yu, I. Bezprozvanny, Presenilins form ER Ca<sup>2+</sup> leak channels, a function disrupted by familial Alzheimer's disease-linked mutations. *Cell* **126**, 981–993 (2006).
- H. Zhang, S. Sun, A. Herreman, B. De Strooper, I. Bezprozvanny, Role of presenilins in neuronal calcium homeostasis. *J. Neurosci.* **30**, 8566–8580 (2010).
- B. De Strooper, W. Annaert, Novel research horizons for presenilins and  $\gamma$ -secretases in cell biology and disease. *Annu. Rev. Cell Dev. Biol.* **26**, 235–260 (2010).
- S. Patel, X. Cai, Evolution of acidic Ca<sup>2+</sup> stores and their resident Ca<sup>2+</sup>-permeable channels. *Cell Calcium* **57**, 222–230 (2015).
- H. Xu, E. Martinoia, I. Szabo, Organellar channels and transporters. *Cell Calcium* **58**, 1–10 (2015).
- L. Avrahami, D. Farfara, M. Shaham-Kol, R. Vassar, D. Frenkel, H. Eldar-Finkelman, Inhibition of glycogen synthase kinase-3 ameliorates  $\beta$ -amyloid pathology and restores lysosomal acidification and mammalian target of rapamycin activity in the Alzheimer disease mouse model. *J. Biol. Chem.* **288**, 1295–1306 (2013).
- R. Dobrowolski, P. Vick, D. Ploper, I. Gumper, H. Snitkin, D. D. Sabatini, E. M. De Robertis, Presenilin deficiency or lysosomal inhibition enhances Wnt signaling through relocalization of GSK3 to the late-endosomal compartment. *Cell Rep.* **2**, 1316–1328 (2012).
- M. Torres, S. Jimenez, R. Sanchez-Varo, V. Navarro, L. Trujillo-Estrada, E. Sanchez-Mejias, I. Carmona, J. C. Davila, M. Vizuete, A. Gutierrez, J. Vitorica, Defective lysosomal proteolysis and axonal transport are early pathogenic events that worsen with age leading to increased APP metabolism and synaptic Abeta in transgenic APP/PS1 hippocampus. *Mol. Neurodegener.* **7**, 59 (2012).
- E. E. Coffey, J. M. Beckel, A. M. Laties, C. H. Mitchell, Lysosomal alkalization and dysfunction in human fibroblasts with the Alzheimer's disease-linked presenilin 1 A246E mutation can be reversed with cAMP. *Neuroscience* **263**, 111–124 (2014).
- R. A. Nixon, J. H. Lee, D. Wolfe, Methods for screening to identify therapeutic agents for Alzheimer's disease and use thereof. U.S. Patent US 15/046,291 (2016).
- M. K. Raychowdhury, S. Gonzalez-Perrett, N. Montalbetti, G. A. Timpanaro, B. Chasan, W. H. Goldmann, S. Stahl, A. Cooney, E. Goldin, H. F. Cantiello, Molecular pathophysiology of mucopolipidosis type IV: pH dysregulation of the mucolipin-1 cation channel. *Hum. Mol. Genet.* **13**, 617–627 (2004).
- Z. Wang, Y. Yan, B. Wang,  $\gamma$ -Secretase genetics of hidradenitis suppurativa: A systematic literature review. *Dermatology* **237**, 698–704 (2021).
- B. Nilius, V. Flockerzi, Mammalian transient receptor potential (TRP) cation channels. Preface. *Handb. Exp. Pharmacol.* **223**, v–vi (2014).
- C. C. Chen, M. Keller, M. Hess, R. Schiffmann, N. Urban, A. Wolfgardt, M. Schaefer, F. Bracher, M. Biel, C. Wahl-Schott, C. Grimm, A small molecule restores function to TRPML1 mutant isoforms responsible for mucopolipidosis type IV. *Nat. Commun.* **5**, 4681 (2014).
- L. Hui, M. L. Soliman, N. H. Geiger, N. M. Miller, Z. Afghah, K. L. Lakpa, X. Chen, J. D. Geiger, Acidifying endolysosomes prevented low-density lipoprotein-induced amyloidogenesis. *J. Alzheimers Dis.* **67**, 393–410 (2019).
- V. Tedeschi, T. Petrozziello, M. J. Sisalli, F. Boscia, L. M. T. Canzoniero, A. Secondo, The activation of Mucolipin TRP channel 1 (TRPML1) protects motor neurons from L-BMAA neurotoxicity by promoting autophagic clearance. *Sci. Rep.* **9**, 10743 (2019).

36. M. Bae, N. Patel, H. Xu, M. Lee, K. Tominaga-Yamanaka, A. Nath, J. Geiger, M. Gorospe, M. P. Mattson, N. J. Haughey, Activation of TRPML1 clears intraneuronal A $\beta$  in preclinical models of HIV infection. *J. Neurosci.* **34**, 11485–11503 (2018).
37. M. McBrayer, R. A. Nixon, Lysosome and calcium dysregulation in Alzheimer's disease: Partners in crime. *Biochem. Soc. Trans.* **41**, 1495–1502 (2013).
38. J. E. Burke, Structural basis for regulation of phosphoinositide kinases and their involvement in human disease. *Mol. Cell* **71**, 653–673 (2018).
39. N. Jin, M. J. Lang, L. S. Weisman, Phosphatidylinositol 3,5-bisphosphate: Regulation of cellular events in space and time. *Biochem. Soc. Trans.* **44**, 177–184 (2016).
40. M. A. Samie, H. Xu, Lysosomal exocytosis and lipid storage disorders. *J. Lipid Res.* **55**, 995–1009 (2014).
41. D. E. Johnson, P. Ostrowski, V. Jaumouille, S. Grinstein, The position of lysosomes within the cell determines their luminal pH. *J. Cell Biol.* **212**, 677–692 (2016).
42. X. Jin, Y. Zhang, A. Alharbi, A. Hanbashi, A. Alhoshani, J. Parrington, Targeting two-pore channels: Current progress and future challenges. *Trends Pharmacol. Sci.* **41**, 582–594 (2020).
43. J. M. Schmitt, G. A. Wayman, N. Nozaki, T. R. Soderling, Calcium activation of ERK mediated by calmodulin kinase I. *J. Biol. Chem.* **279**, 24064–24072 (2004).
44. T. Veeranna, B. Kaji, T. Boland, P. Odrjijn, B. Mohan, S. Basavarajappa, C. Peterhoff, A. Cataldo, A. Rudnicki, N. Amin, B. S. Li, H. C. Pant, B. L. Hungund, O. Arancio, R. A. Nixon, Calpain mediates calcium-induced activation of the erk1,2 MAPK pathway and cytoskeletal phosphorylation in neurons: Relevance to Alzheimer's disease. *Am. J. Pathol.* **165**, 795–805 (2004).
45. Y. Xue, J. Ren, X. Gao, C. Jin, L. Wen, X. Yao, GPS 2.0, a tool to predict kinase-specific phosphorylation sites in hierarchy. *Mol. Cell. Proteomics* **7**, 1598–1608 (2008).
46. C. Bonny, A. Oberson, S. Negri, C. Sauser, D. F. Schorderet, Cell-permeable peptide inhibitors of JNK: Novel blockers of beta-cell death. *Diabetes* **50**, 77–82 (2001).
47. J. H. Lee, M. V. Rao, D. S. Yang, P. Stavrides, E. Im, A. Pensalfini, C. Huo, P. Sarkar, T. Yoshimori, R. A. Nixon, Transgenic expression of a ratiometric autophagy probe specifically in neurons enables the interrogation of brain autophagy in vivo. *Autophagy* **15**, 543–557 (2019).
48. S. Millecamps, J. P. Julien, Axonal transport deficits and neurodegenerative diseases. *Nat. Rev. Neurosci.* **14**, 161–176 (2013).
49. R. A. Nixon, D. S. Yang, J. H. Lee, Neurodegenerative lysosomal disorders: A continuum from development to late age. *Autophagy* **4**, 590–599 (2008).
50. S. Maday, E. L. Holzbaur, Compartment-specific regulation of autophagy in primary neurons. *J. Neurosci.* **36**, 5933–5945 (2016).
51. X. P. Dong, D. Shen, X. Wang, T. Dawson, X. Li, Q. Zhang, X. Cheng, Y. Zhang, L. S. Weisman, M. Dellinger, H. Xu, PI(3,5)P2 controls membrane trafficking by direct activation of mucolipin Ca<sup>2+</sup> release channels in the endolysosome. *Nat. Commun.* **1**, 38 (2010).
52. H. Waller-Evans, E. Lloyd-Evans, Regulation of TRPML1 function. *Biochem. Soc. Trans.* **43**, 442–446 (2015).
53. R. A. Nixon, J. Wegiel, A. Kumar, W. H. Yu, C. Peterhoff, A. Cataldo, A. M. Cuervo, Extensive involvement of autophagy in Alzheimer disease: An immuno-electron microscopy study. *J. Neuropathol. Exp. Neurol.* **64**, 113–122 (2005).
54. D. J. Colacurcio, R. A. Nixon, Disorders of lysosomal acidification—The emerging role of v-ATPase in aging and neurodegenerative disease. *Ageing Res. Rev.* **32**, 75–88 (2016).
55. Y. Miao, G. Li, X. Zhang, H. Xu, S. N. Abraham, A TRP channel senses lysosome neutralization by pathogens to trigger their expulsion. *Cell* **161**, 1306–1319 (2015).
56. X. Li, N. Ryzewski, A. Hider, X. Zhang, J. Yang, W. Wang, Q. Gao, X. Cheng, H. Xu, A molecular mechanism to regulate lysosome motility for lysosome positioning and tubulation. *Nat. Cell Biol.* **18**, 404–417 (2016).
57. R. J. McKenney, M. Vershinin, A. Kunwar, R. B. Vallee, S. P. Gross, LIS1 and NudE induce a persistent dynein force-producing state. *Cell* **141**, 304–314 (2010).
58. P. S. Vaughan, J. D. Leszyk, K. T. Vaughan, Cyttoplasmic dynein intermediate chain phosphorylation regulates binding to dynactin. *J. Biol. Chem.* **276**, 26171–26179 (2001).
59. J. Jie, F. Lohr, E. Barbar, Dynein binding of competitive regulators dynactin and NudE involves novel interplay between phosphorylation site and disordered spliced linkers. *Structure* **25**, 421–433 (2017).
60. J. W. Kim, T. S. Chang, J. E. Lee, S. H. Huh, S. W. Yeon, W. S. Yang, C. O. Joe, I. Mook-Jung, R. E. Tanzi, T. W. Kim, E. J. Choi, Negative regulation of the SAPK/JNK signaling pathway by presenilin 1. *J. Cell Biol.* **153**, 457–464 (2001).
61. E. T. Coffey, Nuclear and cytosolic JNK signalling in neurons. *Nat. Rev. Neurosci.* **15**, 285–299 (2014).
62. A. J. Whitmarsh, The JIP family of MAPK scaffold proteins. *Biochem. Soc. Trans.* **34**, 828–832 (2006).
63. M. M. Fu, J. J. Nirschl, E. L. Holzbaur, LC3 binding to the scaffolding protein JIP1 regulates processive dynein-driven transport of autophagosomes. *Dev. Cell* **29**, 577–590 (2014).
64. C. M. Drerup, A. V. Nechiporuk, JNK-interacting protein 3 mediates the retrograde transport of activated c-Jun N-terminal kinase and lysosomes. *PLoS Genet.* **9**, e1003303 (2013).
65. S. Gowrishankar, Y. Wu, S. M. Ferguson, Impaired JIP3-dependent axonal lysosome transport promotes amyloid plaque pathology. *J. Cell Biol.* **216**, 3291–3305 (2017).
66. S. Y. Yoon, J. E. Choi, J. M. Choi, D. H. Kim, Dynein cleavage and microtubule accumulation in okadaic acid-treated neurons. *Neurosci. Lett.* **437**, 111–115 (2008).
67. M. W. Weible II, N. Ozsarac, M. L. Grimes, I. A. Hendry, Comparison of nerve terminal events in vivo effecting retrograde transport of vesicles containing neurotrophins or synaptic vesicle components. *J. Neurosci. Res.* **75**, 771–781 (2004).
68. A. L. Neisch, T. P. Neufeld, T. S. Hays, A STRIPAK complex mediates axonal transport of autophagosomes and dense core vesicles through PP2A regulation. *J. Cell Biol.* **216**, 441–461 (2017).
69. S. Y. Yoon, J. E. Choi, J. H. Yoon, J. W. Huh, D. H. Kim, BACE inhibitor reduces APP-beta-C-terminal fragment accumulation in axonal swellings of okadaic acid-induced neurodegeneration. *Neurobiol. Dis.* **22**, 435–444 (2006).
70. S. Vergara-Jauregui, J. A. Martina, R. Puertollano, Identification of the penta-EF-hand protein ALG-2 as a Ca<sup>2+</sup>-dependent interactor of mucolipin-1. *J. Biol. Chem.* **284**, 36357–36366 (2009).
71. M. Tsuda, K. H. Seong, T. Aigaki, POSH, a scaffold protein for JNK signaling, binds to ALG-2 and ALIX in Drosophila. *FEBS Lett.* **580**, 3296–3300 (2006).
72. S. Kimura, T. Noda, T. Yoshimori, Dissection of the autophagosome maturation process by a novel reporter protein, tandem fluorescently-tagged LC3. *Autophagy* **3**, 452–460 (2007).
73. A. Choudhury, M. Dominguez, V. Puri, D. K. Sharma, K. Narita, C. L. Wheatley, D. L. Marks, R. E. Pagano, Rab proteins mediate Golgi transport of caveola-internalized glycosphingolipids and correct lipid trafficking in Niemann-Pick C cells. *J. Clin. Invest.* **109**, 1541–1550 (2002).
74. A. L. Ambrosio, J. A. Boyle, S. M. Di Pietro, TPC2 mediates new mechanisms of platelet dense granule membrane dynamics through regulation of Ca<sup>2+</sup> release. *Mol. Biol. Cell* **26**, 3263–3274 (2015).
75. B. Boland, A. Kumar, S. Lee, F. M. Platt, J. Wegiel, W. H. Yu, R. A. Nixon, Autophagy induction and autophagosome clearance in neurons: Relationship to autophagic pathology in Alzheimer's disease. *J. Neurosci.* **28**, 6926–6937 (2008).
76. C. A. Wilson, D. D. Murphy, B. I. Giasson, B. Zhang, J. Q. Trojanowski, V. M. Lee, Degradative organelles containing mislocalized alpha- and beta-synuclein proliferate in presenilin-1 null neurons. *J. Cell Biol.* **165**, 335–346 (2004).
77. L. J. Millet, M. E. Stewart, J. V. Sweedler, R. G. Nuzzo, M. U. Gillette, Microfluidic devices for culturing primary mammalian neurons at low densities. *Lab Chip* **7**, 987–994 (2007).
78. D. M. Wolfe, J. H. Lee, A. Kumar, S. Lee, S. J. Orenstein, R. A. Nixon, Autophagy failure in Alzheimer's disease and the role of defective lysosomal acidification. *Eur. J. Neurosci.* **37**, 1949–1961 (2013).
79. M. W. Walker, E. Lloyd-Evans, A rapid method for the preparation of ultrapure, functional lysosomes using functionalized superparamagnetic iron oxide nanoparticles. *Methods Cell Biol.* **126**, 21–43 (2015).
80. E. Derivery, C. Sousa, J. J. Gautier, B. Lombard, D. Loew, A. Gautreau, The Arp2/3 activator WASH controls the fission of endosomes through a large multiprotein complex. *Dev. Cell* **17**, 712–723 (2009).

**Acknowledgments:** We thank E. Levy, M. Pawlik, and S. DeRosa for maintenance of mouse colonies and A. Kumar for electron microscopy. We also thank M. Mattson for the gift of PSEN1 KI mice. **Funding:** This work was supported by National Institutes of Health grants P01AG017617 and R01AG062376 (to R.A.N.) **Author contributions:** Conceptualization: R.A.N. Methodology: R.A.N. and P.P.Y.L. Investigation: P.P.Y.L., L.Y., J.-H.L., C.N.G., M.J.B., P.S., and C.H. Visualization: P.P.Y.L., L.Y., J.-H.L., C.N.G., M.J.B., and P.S. Supervision: R.A.N. Writing—original draft: R.A.N. and P.P.Y.L. Writing—review and editing: R.A.N., P.P.Y.L., and L.Y. **Competing interests:** The authors declare that they have no competing interests. **Data and materials availability:** All data needed to evaluate the conclusions in the paper are present in the paper and/or the Supplementary Materials.

Submitted 21 May 2021  
Accepted 16 March 2022  
Published 29 April 2022  
10.1126/sciadv.abj5716

## Axonal transport of late endosomes and amphisomes is selectively modulated by local Ca efflux and disrupted by PSEN1 loss of function

Pearl P. Y. LieLang YooChris N. GoulbourneMartin J. BergPhilip StavridesChunfeng HuoJu-Hyun LeeRalph A. Nixon

*Sci. Adv.*, 8 (17), eabj5716. • DOI: 10.1126/sciadv.abj5716

### View the article online

<https://www.science.org/doi/10.1126/sciadv.abj5716>

### Permissions

<https://www.science.org/help/reprints-and-permissions>

Use of this article is subject to the [Terms of service](#)

---

*Science Advances* (ISSN ) is published by the American Association for the Advancement of Science. 1200 New York Avenue NW, Washington, DC 20005. The title *Science Advances* is a registered trademark of AAAS. Copyright © 2022 The Authors, some rights reserved; exclusive licensee American Association for the Advancement of Science. No claim to original U.S. Government Works. Distributed under a Creative Commons Attribution NonCommercial License 4.0 (CC BY-NC).